



k-Space Domain Parallel Transmit Pulse Design

Journal:	<i>Magnetic Resonance in Medicine</i>
Manuscript ID	MRM-20-21508.R1
Wiley - Manuscript type:	Full Paper
Date Submitted by the Author:	10-Oct-2020
Complete List of Authors:	Ma, Jun Gruber, Bernhard; Private, ; Athinoula A Martinos Center for Biomedical Imaging, Radiology Yan, Xinqiang Grissom, William; Vanderbilt University, Biomedical Engineering;
Research Type:	Technical Research
Research Focus:	No specific tissue or organ focus

SCHOLARONE™
Manuscripts

k-Space Domain Parallel Transmit Pulse Design

Jun Ma^{1,2}, Bernhard Gruber^{3,4}, Xinqiang Yan^{1,5}, and William A. Grissom^{1,2,5*}

October 10, 2020

- ¹Vanderbilt University Institute of Imaging Science, Nashville, TN, United States
- ²Department of Biomedical Engineering, Vanderbilt University, Nashville, TN, United States
- ³A. A. Martinos Center for Biomedical Imaging, Massachusetts General Hospital, Harvard Medical School, Charlestown, MA, United States
- ⁴Division MR Physics, Center for Medical Physics and Biomedical Engineering, Medical University Vienna, Vienna, Austria
- ⁵Department of Radiology and Radiological Sciences, Vanderbilt University, Nashville, TN, United States

Word Count: 5630

*Corresponding author:

Will Grissom
Department of Biomedical Engineering
Vanderbilt University
5824 Stevenson Center
Nashville, TN 37235 USA
E-mail: will.grissom@vanderbilt.edu
Twitter: @wgrissom

Submitted to Magnetic Resonance in Medicine for consideration as a Full Paper.

Acknowledgment: This work was supported by NIH grants R01 EB016695 and U01 EB 025162.

Abstract

Purpose: To accelerate the design of (under- or oversampled) multidimensional parallel transmission pulses.

Methods: A k-space domain parallel transmission pulse design algorithm was proposed that produces a sparse matrix relating a complex-valued target excitation pattern to the pulses that produce it, and can be finely parallelized. The algorithm was applied in simulations to the design of 3D SPINS pulses for inner volume excitation in the brain at 7 Tesla. It was characterized in terms of the dependence of computation time, excitation error, and required memory on algorithm parameters, and it was compared to the spatial domain pulse design method in terms computation time, excitation error, Gibbs ringing, and ability to compensate off-resonance.

Results: The proposed algorithm achieved approximately 90% faster pulse design compared to an iterative spatial domain method, with the same number of parallel threads, with the tradeoff of increased excitation error and RMS RF amplitude. It reduced the memory required to store the design matrix by 98% compared to a full matrix solution. Even with a coarse design grid, the algorithm produced patterns that were free of Gibbs ringing. It was similarly sensitive to k-space undersampling as the spatial domain method, and was similarly capable of compensating for off-resonance.

Conclusion: The proposed k-space domain algorithm accelerates and finely parallelizes parallel transmission pulse design, with a modest tradeoff of excitation error and RMS RF amplitude.

Key words: Parallel Transmission; RF pulses; Ultra-high field MRI; RF pulse design; Selective excitation.

1
2
3
4
5 **Introduction**
6

7
8 Multidimensional parallel transmission [1, 2] has been widely investigated for applications includ-
9 ing reduced field-of-view imaging [3, 4], transmit field (B_1^+) inhomogeneity compensation [5, 6],
10 and compensation of susceptibility-induced signal loss [7]. One of the first small-tip-angle pulse
11 design algorithms developed to demonstrate the concept of parallel transmission was formulated in
12 the excitation k-space domain [1]. In that method, a dense system matrix was constructed by apply-
13 ing a Fourier transform to each transmit coil's B_1^+ map, forming a convolution matrix for each coil,
14 and then concatenating the coils' convolution matrices. The pulses were solved by multiplying the
15 regularized pseudoinverse of the system matrix into the target excitation pattern's Fourier trans-
16 form. A spatial domain small-tip-angle parallel transmit pulse design algorithm [8] was proposed
17 soon after, wherein a non-uniform discrete Fourier transform matrix is constructed, duplicated for
18 each transmit coil, and weighted by that coil's B_1^+ map. The weighted matrices are concatenated
19 and the pulses are solved by regularized pseudoinverse of the system matrix or using an iterative
20 method. The spatial domain method is mathematically straightforward and enables flexible mod-
21 eling and compensation of effects such as off-resonance, and incorporation of regions of interest.
22 Since its introduction, most small-tip-angle parallel transmission studies have been formulated in
23 the spatial domain [9, 10].
24
25

26
27
28
29
30
31
32
33
34
35
36
37
38
39
40
41
42
43
44
45
46
47
48
49
50
51
52
53
54
55
56
57
58
59
60
Despite the advantages of the spatial domain approach, it can have prohibitive computational requirements when the number of coils and the number of dimensions become large, for example in three-dimensional [11, 12] or spectral-spatial pulse designs [13–16], when there is a large number of coils [17], and when off-resonance compensation is used. The spatial domain system matrix typically has dimensions $N_s \times (N_c \cdot N_t)$, where N_s is the number of spatial and spectral locations defined in the target excitation pattern, N_c is the number of transmit channels, and N_t is the number of time points in the pulse. Typical values for N_s range from 1,000 for 2D designs to 250,000 for 3D designs, the number of coils varies from 8 to 32 on ultra-high field scanners, and the number of time points varies from 500 to 2,500. Overall, for a 3D design the spatial domain system matrix can occupy upwards of 120 gigabytes of memory, making it infeasible to construct and invert on most

computers. Explicit matrix storage and inversion can be avoided using non-uniform fast Fourier transforms (NUFFTs) to evaluate matrix multiplies, combined with iterative conjugate gradient solvers. In such designs, parallelization can be applied across coils, and GPU-based pulse designs have been described [18]. However, parallelization cannot be applied across iterations; several tens of iterations are commonly used for 3D designs and thousands of iterations can be required for magnitude least-squares [19] or constrained pulse designs [20, 21]. A further challenge for parallel transmit pulse design is that pulses must be computed for each subject, as a pre-scan stage while the subject lies in the scanner.

Here we describe a single-step (non-iterative) small-tip-angle excitation k-space-domain pulse design algorithm with low memory requirements, that can be applied to large pulse design problems with fine parallelization. The algorithm produces a sparse k-space-domain pseudoinverse pulse design matrix that directly relates the Fourier transform of a complex-valued target excitation pattern to the RF pulses that produce it. Once the matrix is built, RF pulses are instantaneously solved by a sparse matrix multiplication, and the matrix need not be recomputed if the target pattern changes. The algorithm takes advantage of the compactness of B_1^+ maps in excitation k-space to independently formulate and solve a parallelizable set of small matrix-vector subproblems to obtain the significant entries of each column or groups of columns of the sparse design matrix.

In the following, we derive the independent solution for each column of the design matrix and introduce a patch-wise parallelization that provides control over the size and accuracy of each subproblem. We describe an efficient method to construct a required matrix of B_1^+ map inner products while maintaining accuracy. A method to incorporate off-resonance correction is also described. The algorithm was characterized and validated in terms of excitation error and computation time, with comparisons to spatial domain designs using NUFFTs and the conjugate gradient algorithm. The application for the designs was a three-dimensional inner-volume excitation using a simulated 24-channel transmit array and a SPINS trajectory [11]. An early account of this work was provided in Ref. [22].

Theory

k-Space-Domain Subproblems

We propose to compute a sparse design matrix \mathbf{W} that directly maps the Fourier transform of a desired spatial excitation pattern to a vector of RF pulses that together produce the pattern, as:

$$\mathbf{b} = \mathbf{W}\mathcal{F}(\mathbf{d}), \quad [1]$$

where \mathbf{b} is a vector of concatenated multi-channel RF pulses with length $N_t N_c$, where N_t and N_c are the numbers of time points and channels, respectively, and $\mathcal{F}(\mathbf{d})$ is a length- N_s vector containing the Fourier transform of the complex-valued target k-space excitation pattern \mathbf{d} . \mathbf{W} has dimensions $N_t N_c \times N_s$. Once the entries of \mathbf{W} are computed, the RF design problem can be instantaneously solved by a sparse matrix multiplication. Here we describe how to break down the problem of constructing \mathbf{W} into a set of smaller independent subproblems that can be solved in parallel.

The columns of \mathbf{W} can be solved independently, based on the observation that if the desired k-space pattern is a delta function at a k-space location \vec{k}_j ($1 \leq j \leq N_s$), then only the j -th column \mathbf{w}_j of \mathbf{W} is required to relate the desired k-space pattern to the desired RF pulse. In this case, the vector \mathbf{w}_j is identical to the desired RF. Therefore, the problem of finding the j -th column \mathbf{w}_j of \mathbf{W} can be stated as: what should the RF pulse samples be to generate a unit delta function at the location \vec{k}_j in k-space, and zeros elsewhere? Mathematically, the relationship that should be satisfied by the weights in column \mathbf{w}_j can be expressed as:

$$\delta(\vec{k} - \vec{k}_j) = \sum_{i=1}^{N_t} \sum_{c=1}^{N_c} w_c(\vec{k}_i) s_c(\vec{k} - \vec{k}_i), \quad [2]$$

where i indexes time points in the pulses' excitation k-space trajectory, and c indexes channels. $w_c(\vec{k}_i)$ is the $((c-1)N_t + i)$ -th element of the \mathbf{w}_j vector, and $s_c(\vec{k} - \vec{k}_i)$ is the Fourier transform of channel- c 's B_1^+ map, shifted to be centered at excitation k-space location \vec{k}_i . Equation 2 can be restated in matrix-vector form as:

$$\mathbf{S}\mathbf{w}_j = \delta_j, \quad [3]$$

where \mathbf{S} is a $N_s \times N_c N_t$ matrix containing values of $s_c(\vec{k} - \vec{k}_i)$ for all c and i , and δ_j is a vector containing a one in the entry corresponding to excitation k-space location \vec{k}_j , and zeros in all other entries. The regularized pseudoinverse solution for w_j is:

$$w_j = (\mathbf{S}^H \mathbf{S} + \lambda \mathbf{I})^{-1} s_j^H \quad [4]$$

where s_j^H is the conjugate transpose of the j -th row of \mathbf{S} .

If all points on the excitation k-space trajectory are considered in Equation 2, then there is no reduction in computation compared to a conventional pseudoinverse-based pulse design. However, because B_1^+ maps are localized near $\vec{k} = 0$ in excitation k-space, only a small number ($\ll N_t$) of trajectory points near the target location \vec{k}_j can contribute significantly to the excitation pattern at \vec{k}_j or its neighbors, and therefore need to be considered in the subproblem; all other trajectory points can be ignored. This means Equation 2 can be modified to:

$$\delta(\vec{k} - \vec{k}_j) = \sum_{\vec{k}_i \in \mathbb{N}} \sum_{c=1}^{N_c} w_c(\vec{k}_i) s_c(\vec{k} - \vec{k}_i), \quad [5]$$

where \mathbb{N} is the set of trajectory points in the vicinity of \vec{k}_j . In this work ‘inclusion width’ is defined as the distance, in phase cycles over the excitation field-of-view (cycles/FOV), from each target location \vec{k}_j within which all trajectory points are accrued into \mathbb{N} . This reduced set of trajectory points reduces the column dimension of \mathbf{S} and both dimensions of $\mathbf{S}^H \mathbf{S}$, and implies that the design matrix \mathbf{W} is sparse. Figure 1a illustrates a target point \vec{k}_j for a two-dimensional pulse design, and the nearby points on the trajectory that need to be included in the solution for w_j for an inclusion width of 4 cycles/FOV.

The \mathbf{W} matrix columns w_j can be solved in parallel one-at-a-time or patch-wise, wherein all target points in a patch share the same $\mathbf{S}^H \mathbf{S}$ matrix, and their s_j^H vectors are concatenated in the column dimension to form a matrix in Equation 4. An illustration of a 4×4 patch and its included trajectory points is shown in Figure 1b, for a two-dimensional spiral pulse design. The inclusion width is also 4 cycles/FOV from any target point in the patch, so all the excitation trajectory points within a 12×12 cycles/FOV square are included in the calculation.

Efficient $S^H S$ matrix construction

Constructing the $S^H S$ matrix by first constructing S is computationally expensive because it requires each channel's B_1^+ map to be shifted to each trajectory location \vec{k}_i by phase modulation followed by Fourier transform, or by Fourier transform followed by interpolation. Furthermore, the matrix multiplication between S^H and S is also computationally intensive due to the potentially large row dimension of S , if the zero excitation condition is enforced on a large grid of points around each \vec{k}_j . The computational costs can be reduced by truncating the B_1^+ maps in k-space, but this introduces large errors. Instead, inspired by the non-Cartesian GRAPPA method of Ref [23], we propose to construct the Hermitian $S^H S$ matrix directly via interpolation of the Fourier transforms of inner products of pairs of B_1^+ maps. The $S^H S$ matrix can be written in block form as:

$$S^H S = \begin{pmatrix} S_1^H S_1 & \cdots & S_1^H S_{N_c} \\ \vdots & \ddots & \vdots \\ S_{N_c}^H S_1 & \cdots & S_{N_c}^H S_{N_c} \end{pmatrix}, \quad [6]$$

where each sub-matrix $S_i^H S_j$ contains inner products of the Fourier transforms of channel i and channel j 's B_1^+ maps, after they are shifted to be centered different points on the excitation trajectory corresponding to the row and column indices of the sub-matrix. These inner products can be calculated by interpolating the Fourier transform of the inner product of channel i and channel j 's B_1^+ maps. In other words, each element in the Hermitian matrix $S_i^H S_j$ is the vector sum of channel i and channel j 's shifted k-space B_1^+ maps, which is also a single point of their k-space convolution. Via the multiplication property of the Fourier transform, this convolution in k-space can be calculated from the Fourier transform of the dot product of the two spatial domain B_1^+ maps. For further details, please refer to Ref. [23].

Since $S^H S$ and its sub-matrices are Hermitian, we only need to find the values within the lower triangle of the matrix, which are the sub-matrices $S_i^H S_j$ with $i > j$ that are themselves lower triangular. The elements of a given sub-matrix $S_i^H S_j$ are interpolated from a densely sampled Fourier transform of the dot product of the spatial domain B_1^+ maps of the i -th and j -th channels. The

(m, n)-th element is the value interpolated at a position $\vec{k}_m - \vec{k}_n$ away from DC, where \vec{k}_m and \vec{k}_n are the excitation k-space trajectory locations corresponding to row m and column n . Compared to phase-modulating and Fourier transforming each channel's B_1^+ map for each point on the trajectory which would require $N_t N_c$ Fourier transforms, to solve all the columns of \mathbf{W} the total number of Fourier transforms needed in this efficient method is $N_c(N_c + 1)/2$. The storage size is also much smaller, and the matrix multiplication between \mathbf{S}^H and \mathbf{S} is avoided.

Off-Resonance Compensation

Off-resonance compensation is common in spatial-domain parallel pulse designs [8], but has not been previously implemented in a k-space-domain design. Spatial domain designs based on NUFFTs make use of an approximate time-segmented model for the off-resonance term [24], which decouples the space- and time-dependence of off-resonant phase accrual into the product of space- and time-dependent terms, which are applied on either side of the NUFFT operator. Here we show how a time-segmented off-resonance model can be incorporated in the proposed k-space-domain algorithm. Mathematically, the time-segmented model is given by:

$$e^{i\Delta\omega(\vec{x}_j)(t_i-T)} \approx \sum_{l=1}^L b_l(t_i) h_l(\vec{x}_j), \quad [7]$$

where $\Delta\omega(\vec{x}_j)$ is the off-resonance frequency at \vec{x}_j , i indexes time points in the pulse, T is the pulse duration, and l indexes the L time segments, where L is typically between 4 and 8. The $b_l(t_i)$ functions are temporal interpolators that multiply into the RF samples and are determined by numerical optimization as described in Ref. [24], and $h_l(\vec{x}_j) = e^{i\Delta\omega(\vec{x}_j)t_l}$ are the off-resonance phase shifts applied to the excitation patterns produced by the RF pulse time segments centered at time points $\{t_l : l = 1, \dots, L\}$. The time-segmented off-resonance model can be incorporated into Equation 2 as:

$$\delta(\vec{k} - \vec{k}_j) = \sum_{l=1}^L \sum_{i=1}^{N_t} \sum_{c=1}^{N_c} w_c(\vec{k}_i) b_l(t_i) \tilde{s}_{cl}(\vec{k} - \vec{k}_i), \quad [8]$$

where $\tilde{s}_{cl}(\vec{k})$ is the Fourier transform of the product of channel c 's B_1^+ map and time segment l 's off-resonance phase shift $h_l(\vec{x}_j)$. We can then write the equivalent of Equation 3 with the off-

resonance model:

$$\sum_{l=1}^L \mathbf{S}_l \text{diag}(b_l(t_i)) \mathbf{w}_j = \delta_j, \quad [9]$$

where the matrix \mathbf{S}_l is now formed from the $N_c L$ Fourier transforms of the B_1^+ map and $h_l(\vec{x}_j)$ products. Efficient construction of the $\mathbf{S}^H \mathbf{S}$ matrix follows much the same procedure as without off-resonance except that with off-resonance, the elements of each sub-matrix $\mathbf{S}_i^H \mathbf{S}_j$ in Equation 6 are interpolated from $L(L+1)/2$ Fourier transformed maps, and the interpolated values are weighted by the temporal interpolators for each pair of multiplied time segments before they are summed. Compared to constructing $\mathbf{S}^H \mathbf{S}$ without off-resonance, taking off-resonance into account increases the total number of FFT operations from $N_c(N_c+1)/2$ to $N_c L(N_c L+1)/2$, and increases the number of interpolations needed for each sub-matrix element from 1 to $L(L+1)/2$. However, we note that only adjacent time segments with overlapping temporal interpolators at a given time point need to be considered when calculating the elements of $\mathbf{S}^H \mathbf{S}$ corresponding to that time point.

Methods

Design and Simulation Setup

Simulations were performed to validate and characterize the proposed k-space domain parallel transmit pulse design method, with comparisons to a least-squares spatial-domain design [8]. RF pulses were designed for a simulated 24-channel loop transmit array (Figure 2) that is being built for a 7 Tesla scanner optimized for imaging the human cortex. 24-channel complex-valued B_1^+ maps used in the pulse designs were simulated in a male human head model using Ansys High Frequency Structure Simulator (Canonsburg, PA, USA) with 1.5 mm isotropic resolution. Figure 3a shows the target pattern for all pulse designs which comprised an ellipse centered on the ventricles with AP/HF/LR semi-axes of 4.8/3.2/3.2 cm, with zero phase. The pattern was smoothed by a Fermi filter that was applied in the frequency domain to match the target pattern's effective resolution to the excitation k-space trajectory's 5 mm resolution. This choice of target pattern was motivated

by imaging applications for the 7 Tesla scanner in which midbrain signals will be saturated for high-resolution, highly-accelerated imaging of the cortex. Pulses were designed to excite the entire ellipse and achieve zero excitation in voxels in the cerebrum but outside the ellipse. The smoothed target pattern and the B_1^+ maps were downsampled from their original $128 \times 128 \times 96$ grids (1.5 mm isotropic resolution) to $64 \times 64 \times 48$ grids (3 mm isotropic resolution), and RF designs were performed with the $64 \times 64 \times 48$ grid size.

A SPINS excitation k-space trajectory [11] (Figure 3b) with 5 mm max resolution was used for the designs. The SPINS trajectory comprised three segments with radii ranging between 1-0.625, 0.625-0.375, and 0.375-0 cycles/cm, respectively. The number of polar and azimuthal rotations were 15.5/2.125, 20.66/2.833, 15.5/2.125 for each segment, respectively. The SPINS trajectories were first designed analytically and the final gradient waveforms and excitation k-space trajectories were designed from them using the minimum-time gradient waveform design method [25], for a 15 μ s dwell time and subject to the scanner's gradient amplitude and slew rate constraints of 200 mT/m and 700 T/m/s, respectively (Figure 3c). The durations of the three segments after minimum-time gradient design were 4.174, 4.326, and 1.5 ms, respectively. With the exception of the simulations across undersampling factors, all pulse designs used this 10 ms trajectory. With this trajectory and the $64 \times 64 \times 48$ design grid size, the dimensions of the \mathbf{W} matrix were 16,632 RF pulse samples, by 196,608 target k-space locations.

All pulse designs and Bloch equation simulations were performed in MATLAB (Mathworks, Natick, MA, USA). For spatial domain designs, RF pulses were solved using an iterative least-squares conjugate-gradient descent method with 35 iterations, which was accelerated by NUFFTs [26]. Except for the off-resonance-compensated designs described below, all spatial domain designs were parallelized using 16 threads that simultaneously computed the forward and backward NUFFTs across transmit coils. The proposed k-space domain algorithm was implemented based on code for the non-Cartesian GRAPPA method of Ref. [23], as a function that takes as input the B_1^+ maps and a normalized excitation k-space trajectory. Within that function the Fourier transforms of the B_1^+ products are calculated, and a C-based MATLAB Executable (MEX) function

is invoked to solve for the non-zero elements of each column of \mathbf{W} , with linear interpolation of the Fourier transforms of the B_1^+ map products to obtain the entries of the $\mathbf{S}^H \mathbf{S}$ matrices. Those elements are then inserted into a sparse \mathbf{W} matrix, which is the single output of the main function. Parallelization was implemented across patches within the C-based MEX function using the Open Multi-Processing (OpenMP) library. The final pulses are calculated by multiplying the sparse \mathbf{W} matrix into the Fourier transform of the target pattern. This code, the B_1^+ maps, and a demo script are available at <https://github.com/wgrissom/kpTx>. All pulse designs were performed on a server (Colfax International, Santa Clara, CA, USA) with 512 GB RAM and two 24-core 2.1 GHz Intel Xeon CPUs which provide up to 94 threads (Intel Corporation, Santa Clara, CA, USA). Designs were performed five times for each case, and the mean computation time was recorded. For the k-space domain designs, the design time comprised the time to compute the sparse \mathbf{W} matrix, and the time to multiply it into the target pattern to obtain the pulses. The resulting pulses were Bloch equation-simulated and compared to the target pattern on the finer $128 \times 128 \times 96$ grid to capture Gibbs ringing. When calculating excitation errors, the magnitude root-mean-square error (RMSE) was calculated in voxels within the cerebrum, except for an ≈ 5 mm-thick transition band around the edge of the elliptical target region.

k-Space Algorithm Parameters

To evaluate how accuracy and compute time depend on k-space-domain design parameters and parallelization, pulse designs were done across numbers of threads (i.e., how many patches were solved simultaneously; 1 to 32), patch widths (1 to 16 cycles/FOV), and inclusion widths (2 to 8 cycles/FOV). The number of threads were varied while holding the patch width and inclusion width both at 4 cycles/FOV. The patch width was varied while holding the number of threads at 16, and the inclusion width at 4 cycles/FOV, and the inclusion width was varied (2, 4, 6, and 8 cycles/FOV) while holding the number of threads at 16, and the patch width at 4 and 8 cycles/FOV. The sizes of the \mathbf{W} matrices were also recorded, holding patch width constant at 4 cycles/FOV and varying the inclusion width.

L-Curves

To compare the tradeoff between excitation error (measured by root-mean-square error) and integrated RF root-mean-square (RMS) amplitude for spatial and k-space domain designs, pulse designs were repeated while varying Tikhonov regularization parameters (λ in Equation 4) over five orders of magnitude. The k-space domain designs were repeated four times to investigate the two main sources of error: finite patch and inclusion widths, and B_1^+ map product interpolation when building the $S^H S$ matrices. Specifically, for each λ a design was performed using patch and inclusion widths of four ('Patch/Inclusion Widths = 4') with interpolated B_1^+ map products ('Interpolated Matrices'), patch and inclusion widths covering the entire design grid ('Patch/Inclusion Widths = ∞ ') with interpolated B_1^+ map products, patch and inclusion widths of four without B_1^+ map product interpolation ('Exact Matrices'; B_1^+ maps were phase-modulated to each trajectory location before Fourier transform), and patch and inclusion widths covering the entire design grid without B_1^+ map product interpolation. Note that the last case is equivalent to the original k-space domain method of Ref. [1]. For each design, flip angle RMSE (calculated using the spatial domain NUFFT) and root-mean-square RF amplitude were recorded.

Gibbs Ringing

Gibbs ringing commonly arises in spatial domain parallel pulse designs when the resolution of the design grid is similar to that of the excitation k-space trajectory. The proposed k-space-domain method is implemented without wraparound or circulant end conditions in excitation k-space, so Gibbs ringing should be suppressed even when using a design grid that is only slightly wider than the trajectory. To demonstrate this, the target pattern and B_1^+ maps were further down-sampled to $32 \times 32 \times 24$ (6 mm isotropic-resolution), and the outermost leaves of the SPINS trajectory which had duration 2.1 ms were excluded so that the maximum excitation resolution matched the 6 mm target pattern and B_1^+ map resolution. Using this shorter 7.9 ms trajectory, pulses were designed by the spatial domain method using both $32 \times 32 \times 24$ and $64 \times 64 \times 48$ grid sizes, and by the k-space-domain method for $32 \times 32 \times 24$ grid size. The Tikhonov regularization parameters for the

1
2
3
4
5
6
7
8
9
10
11
12
13
14
15
16
17
18
19
20
21
22
23
24
25
26
27
28
29
30
31
32
33
34
35
36
37
38
39
40
41
42
43
44
45
46
47
48
49
50
51
52
53
54
55
56
57
58
59
60

32×32×24 designs were set so that the RMS RF amplitudes produced by the k-space domain and spatial domain designs matched. The designed pulses were then evaluated against the target pattern using the 128×128×96 grid size, to visualize the ringing.

Excitation k-Space Undersampling

An important application of parallel transmission is the reduction of multidimensional pulse durations by excitation k-space undersampling. To compare the spatial domain and k-space domain methods across undersampling factors, the number of polar and azimuthal rotations in each segment of the SPINS trajectory were increased and reduced relative to the reference design described above, by factors of 0.5, 2, and 4. That is, for a reduction factor of 0.5, the number of polar and azimuthal rotations in the trajectory were doubled for each of the three segments, and they were halved for a reduction factor of 2. This yielded pulse durations of 20.5 ms (reduction factor 0.5), 5.3 ms (reduction factor 2), and 2.6 ms (reduction factor 4).

Off-Resonance

To compare the off-resonance-compensated k-space domain designs with off-resonance-compensated spatial domain designs, we incorporated a Gaussian ($\sigma = 3$ cm) field map centered above the frontal sinus, which was designed to mimic the characteristic susceptibility-induced B_0 inhomogeneity in this part of the human brain. The field maps were then scaled so that the maximum off-resonance reached +200 Hz and +400 Hz. A time-segmented approximate off-resonance model was calculated using the method of Ref. [24] with $L = 4$ time segments, and this model was used in both spatial domain and k-space domain designs. Both spatial domain and k-space domain designs used 32 parallel threads.

Results

Figure 4 shows simulated excitation patterns and error maps for the reference spatial and k-space domain designs. Both designs were performed with 16 parallel threads and the $64 \times 64 \times 48$ grid size (3 mm isotropic resolution), and the excitation patterns were evaluated against the target pattern on a $128 \times 128 \times 96$ grid size (1.5 mm iso-resolution). The k-space domain design used patch and inclusion widths of 4. The calculated root-mean-squared errors (RMSEs) were 2.42% (spatial domain) and 2.68% (k-space domain), respectively. For both design methods, most of the errors appeared at the edges of the transition band, and errors elsewhere were lower than 5% of the target flip angle. This indicates uniform inner volume excitation while maintaining the outer volume intact. The parallelized k-space domain design required 2.9 seconds computation versus 31.8 seconds for the spatial domain method, a 91% decrease.

k-Space Algorithm Parameters

Figure 5a plots mean computation time versus number of parallel threads, holding the patch and inclusion widths fixed at 4 cycles/FOV. The computation time decreased rapidly with increasing thread number up to 12 threads, and then plateaued, likely due to the overhead involved in initiating threads after that point. Based on this result, the number of threads was held fixed at 16 for subsequent designs when off-resonance was not compensated.

Figure 5b plots mean computation time and RMSE with different patch widths. The computation time decreased up to a patch width of 4 cycles/FOV (corresponding to $4^3 = 64$ simultaneously solved columns of \mathbf{W}) and then increased sharply for larger patch widths. RMSE decreased slowly as the patch width increased since the number of excitation trajectory points included in the calculation of weights for each target point increases on average (and especially for target locations in the middle of each patch) as the patch width increases, even when the inclusion width stays fixed. Based on this result, a patch width of 4 cycles/FOV was used for subsequent designs.

Figure 5c plots mean computation time and RMSE with different inclusion widths. The solid lines and dashed lines were obtained with patch widths of 4 and 8 cycles/FOV, respectively. Com-

putation time increased and error decreased with increasing inclusion width, since more excitation trajectory points were included in each target location’s calculation for increasing inclusion width, corresponding to an increased $S^H S$ matrix size. The RMSE was only slightly lower for a patch width of 8 versus 4 cycles/FOV, but the computation time was much higher for 8 cycles/FOV, across all inclusion widths. The knees in the curves occurred approximately at an inclusion width of 4 cycles/FOV, so this value was used in subsequent designs.

Table 1 lists the size of the final matrix W in gigabytes, versus inclusion width. As inclusion width increases, more excitation trajectory points are used in the solution of the weights for each target location, until the entire trajectory is used for each location (inclusion width = ∞ in the table), corresponding to a full solution. With the inclusion width of 4 cycles/FOV used here, the matrix size was 98% smaller than that of a full solution.

L-Curves

Figure 6 plots flip angle RMSE versus RF RMS amplitude for the spatial domain method and different configurations of the k-space domain method. The spatial domain method achieves the best overall tradeoff between error and RMS amplitude (dashed black curve), which is matched by the k-space domain method when all target locations are solved simultaneously with all excitation trajectory points included and exact $S^H S$ matrix construction (orange curve). When the inclusion and patch widths are limited to 4 cycles/FOV but the $S^H S$ matrices are still constructed exactly, there is an increase in error and RMS amplitude (solid blue curve). However, a larger penalty is incurred by interpolating the entries of the $S^H S$ matrices (dashed orange curve) than by limiting the inclusion and patch widths. Combining interpolation of the $S^H S$ matrix entries and patch and inclusion widths of 4 cycles/FOV yield the dashed blue curve, which has a higher error and RF amplitude than when interpolation or small patch and inclusion widths are used alone. Overall, these results and the results in Figure 5 and Table 1 show that the k-space domain method allows a tradeoff between computation time and memory usage versus excitation error and RMS RF amplitude. The dots on the spatial domain and k-space domain curves indicate the knees of the

curves corresponding to the λ values used for the designs in Figures 4, 5, 8, and 9. Note that the RMSE's in Figure 6 are slightly lower for the spatial domain designs and slightly higher for the k-space domain designs compared to other figures, because the flip angle errors in Figure 6 were calculated using spatial domain NUFFTs instead of Bloch equation simulations, to provide a more direct measure of the design error.

Gibbs Ringing

Figure 7a shows slices of the excitation error pattern produced by pulses designed by the spatial domain method on a $32 \times 32 \times 24$ grid, which were Bloch-simulated on the original $128 \times 128 \times 96$ grid. There is significant Gibbs ringing in the pattern (indicated by the red arrows), and the pulses incur a higher RMSE (4.64%) than pulses designed using either the spatial domain method with a finer $64 \times 64 \times 48$ grid (2.66%; Figure 7b) or the k-space domain method with a $32 \times 32 \times 24$ grid (3.00%; Figure 7c). Gibbs ringing is not apparent in either the $64 \times 64 \times 48$ spatial domain error pattern or the $32 \times 32 \times 24$ k-space domain error pattern. The RMS RF amplitudes of the low-resolution designs were both 0.005. Note that the error of the $64 \times 64 \times 48$ spatial domain design is slightly higher than designs presented in other figures due to the lower-resolution excitation trajectory. From a spatial domain point of view, the Gibbs ringing in the low-resolution spatial domain design was caused by the design's inability to observe and limit the ringing in the low-resolution design grid. From a k-space domain point of view, the Gibbs ringing was due to implicit circulant end conditions at the edges of excitation k-space, which led RF samples at one edge of k-space to wrap-around and affect target locations at the opposite edge of k-space. This effect is mitigated using a high-resolution spatial domain design grid, as illustrated in Figure 7b. However, even for a low-resolution k-space domain design there is no wrap-around effect in excitation k-space because the trajectory points that are incorporated in solution for each patch are explicitly specified to be those in the immediate vicinity of that patch, without circulant end conditions.

Excitation k-Space Undersampling

Figure 8 compares excitation error patterns produced by spatial domain-designed pulses (top row) and k-space domain-designed pulses (middle row), for different trajectory reduction factors which resulted in the SPINS trajectories plotted in the third row. For each design the k-space domain-designed pulses had higher error, but error increased smoothly with increasing reduction factor, as it did for the spatial domain designs. Figure 8 also reports mean computation time for each design. The spatial domain times were fairly constant across reduction factors despite the decreasing number of time samples with increasing reduction factor. This was because the size of the FFT operations in the NUFFTs depended not on the length of the trajectory but on the size of the target pattern which did not change with reduction factor, and the FFT operations dominated the NUFFT computation times relative to the gridding operations. Conversely, the k-space domain times did decrease with reduction factor since the number and sizes of the $S^H S$ matrices depend on the trajectory length.

Off-Resonance

Figure 9a shows the off-resonance maps containing a Gaussian distortion which was centered above the frontal sinus, and scaled to peak amplitudes of 0, 200, and 400 Hz for the pulse designs and Bloch simulations. Figure 9b shows excitation error patterns and RMSEs for spatial domain designs with off-resonance compensation, and k-space domain designs without and with off-resonance compensation. Without off-resonance compensation, the k-space domain-designed pulses produced large ($> 10\%$ of M_0) excitation errors both inside and outside the target ellipse. When the off-resonance map was incorporated in the spatial domain and k-space domain designs, the distortion was nearly fully corrected when it had a peak amplitude of 200 Hz. When the map was scaled to a peak of 400 Hz, some large errors remained, with the k-space domain-designed pulses achieving slightly lower RMSE.

Discussion

Summary

A small-tip-angle k-space domain parallel transmit pulse design algorithm was proposed that divides up the calculation of a matrix relating a target excitation pattern to the pulses that produce it into a set of independent problems for patches of target excitation k-space locations, each of which is influenced by a local neighborhood of points on the excitation k-space trajectory. The division of the problem into patches of target locations creates an opportunity for fine parallelization, while the limited neighborhood sizes lead to small problem sizes for each patch. Compared to the original k-space-based algorithm of Ref. [1], the L-curve and matrix size results showed that the new algorithm produces much smaller matrix sizes that can be calculated more quickly, with the tradeoff of increased excitation error or RF power. Results showed that the algorithm also enables compensation of off-resonance which has not previously been described in a k-space domain design. Compared to a spatial domain design, the new algorithm is non-iterative and can be finely parallelized to achieve shorter design times, and results showed that it can use coarser target grid sizes while avoiding Gibbs ringing, again with the tradeoff of increased excitation error or RF power. The performance of off-resonance-compensated spatial domain and k-space domain pulse designs was similar, and the methods were similarly sensitive to excitation k-space undersampling. While all the pulse designs in this work used 3D SPINS trajectories, the method can be applied in any number of dimensions and with any excitation k-space trajectory. The MATLAB implementation described can be used for any two- or three-dimensional pulse design without modification.

Applications and Extensions

This work was initially motivated by the observation that spatial domain parallel pulse designs can be very slow for 3D problems with large grid sizes, requiring many iterations with considerable computation per iteration. It is anticipated that the proposed k-space domain algorithm will be most useful for these types of large >2D problems, which include 3D spatial designs [11, 12] and 2D

and 3D spatial-spectral designs [13–16] where full matrix construction and inversion is infeasible due to the problem size, and an iterative design can require several minutes to solve. Furthermore, unlike an iterative spatial domain design the proposed algorithm does not need to be repeated if the target pattern changes. This means it could have a considerable computational speed advantage for Gerchberg-Saxton magnitude least-squares pulse designs [3, 19] which alternate between designing pulses and updating a complex-valued target pattern. Such a design method would allow the user to specify only the magnitude of the target pattern, rather than magnitude and phase as was required in this work. The method could also be used to initialize spatial-domain designs to reduce the number of iterations required to reach a target cost. Finally, while simple Tikhonov RF power regularization was used in the designs presented here, more sophisticated regularization could be incorporated to, e.g., control peak RF power via adaptive regularization [27], or to enforce array compression by projecting the weights into the null space of a compression matrix [28], among other applications [9, 10]. In such designs, it would be beneficial to pre-compute and store the lower triangular elements of the $S^H S$ matrices so they need not be re-computed as the regularization changes over iterations. Peak power could also be controlled in k-space domain designs using parallel transmission VERSE [29] or the iterative re-VERSEit technique [30]. It is not yet clear whether or how hard constraints on SAR and peak- and integrated-power could be directly incorporated in the k-space method, as in Refs [20] and [21]. It may also be possible to use the k-space domain method to rapidly design large-tip-angle pulses via the direct linear class of large-tip-angle pulses method [31] or the additive angle method [32]; the latter alternates between small-tip-angle designs that could be solved by the k-space method, and Bloch simulations to update the target pattern.

Conclusion

The proposed k-space domain algorithm accelerates and finely parallelizes parallel transmission pulse design, with a modest tradeoff of excitation error and RMS RF amplitude.

Acknowledgments

The authors would like to thank Tianrui Luo (University of Michigan) for helpful discussions regarding Ref [23].

For Peer Review

References

[1] Katscher U, Börnert P, Leussler C, van den Brink JS. Transmit SENSE. *Magn Reson Med* 2003;49:144–150.

[2] Zhu Y. Parallel excitation with an array of transmit coils. *Magn Reson Med* 2004;51:775–784.

[3] Malik SJ, Hajnal JV. Phase relaxed localized excitation pulses for inner volume fast spin echo imaging. *Magn Reson Med* 2016;76:848–861.

[4] Mooiweer R, Sbrizzi A, Raaijmakers AJE, Van den Berg CAT, Luijten PR, Hoogduin H. Combining a reduced field of excitation with SENSE-based parallel imaging for maximum imaging efficiency. *Magn Reson Med* 2016;78:88–96.

[5] Zhang Z, Yip CY, Grissom W, Noll DC, Boada FE, Stenger VA. Reduction of transmitter B1 inhomogeneity with transmit SENSE slice-select pulses. *Magn Reson Med* 2007;57:842–847.

[6] Cloos MA, Boulant N, Luong M, Ferrand G, Giacomini E, Le Bihan D, Amadon A. k_T -Points: Short three-dimensional tailored RF pulses for flip-angle homogenization over an extended volume. *Magn Reson Med* 2011;67:72–80.

[7] Deng W, Yang C, Alagappan V, Wald LL, Boada FE, Stenger VA. Simultaneous z-shim method for reducing susceptibility artifacts with multiple transmitters. *Magn Reson Med* 2009;61:255–259.

[8] Grissom WA, Yip CY, Zhang Z, Stenger VA, Fessler JA, Noll DC. Spatial domain method for the design of RF pulses in multicoil parallel excitation. *Magn Reson Med* 2006;56:620–9.

[9] F. Padormo, A. Beqiri, J. V. Hajnal, and S. J. Malik. Parallel transmission for ultrahigh-field imaging. *NMR Biomed* 2016; 29(9):1145–1161.

[10] C. M. Deniz. Parallel transmission for ultrahigh field MRI. *Top Magn Reson Imaging* 2019; 28(3):159–171.

- [11] Malik SJ, Keihaninejad S, Hammers A, Hajnal JV. Tailored excitation in 3D with spiral nonselective (SPINS) RF pulses. *Magn Reson Med* 2012;67:1303–1315.
- [12] Davids M, Schad LR, Wald LL, Guerin B. Fast three-dimensional inner volume excitations using parallel transmission and optimized k-space trajectories. *Magn Reson Med* 2016; 76:1170–1182.
- [13] K. Setsompop, V. Alagappan, B. A. Gagoski, A. Potthast, F. Hebrank, U. Fontius, F. Schmitt, L. L. Wald, and E. Adalsteinsson. Broadband slab selection with b_1^+ mitigation at 7T via parallel spectral-spatial excitation. *Magn Reson Med* 2009; 61:493–500.
- [14] S. J. Malik, D. J. Larkman, D. P. O'Regan, and J. V. Hajnal. Subject-specific water-selective imaging using parallel transmission. *Magn Reson Med* 2010; 63(4):988–997.
- [15] Stenger VA, Boada FE, Noll DC. Three-dimensional tailored RF pulses for the reduction of susceptibility artifacts in T_2^* -weighted functional MRI. *Magn Reson Med* 2000;44:525–531.
- [16] Yang C, Deng W, Alagappan V, Wald LL, Stenger VA. Four-dimensional spectral-spatial RF pulses for simultaneous correction of B_1^+ inhomogeneity and susceptibility artifacts in T_2^* -weighted MRI. *Magn Reson Med* 2010;64:1–8.
- [17] Orzada S, Solbach K, Gratz M, Brunheim S, Fiedler TM, Johst S, Bitz AK, Shooshtary S, Abuelhaija A, Voelker MN, Rietsch SHG, Kraff O, Maderwald S, Flöser M, Oehmigen M, Quick HH, Ladd ME. A 32-channel parallel transmit system add-on for 7T MRI. *PLOS ONE* 2019;14:1–20.
- [18] Deng W, Yang C, Stenger VA. Accelerated multidimensional radiofrequency pulse design for parallel transmission using concurrent computation on multiple graphics processing units. *Magn Reson Med* 2011;65:363–369.
- [19] Setsompop K, Wald L, Alagappan V, Gagoski B, Adalsteinsson E. Magnitude least squares

optimization for parallel radio frequency excitation design demonstrated at 7 Tesla with eight channels. *Magn Reson Med* 2008;59:908–915.

[20] Brunner DO, Pruessmann KP. Optimal design of multiple-channel RF pulses under strict power and SAR constraints. *Magn Reson Med* 2010;63:1280–1291.

[21] Hoyos-Idrobo A, Weiss P, Massire A, Amadon A, Boulant N. On variant strategies to solve the magnitude least squares optimization problem in parallel transmission pulse design under strict SAR and power constraints. *IEEE Trans Med Imag* 2014;33:739–748.

[22] Grissom WA. k-Space domain parallel transmit pulse design. In *Proceedings 26th Scientific Meeting, International Society for Magnetic Resonance in Medicine, Paris. 2018*; p. 3396.

[23] Luo T, Noll DC, Fessler JA, Nielsen JF. A GRAPPA algorithm for arbitrary 2D/3D non-Cartesian sampling trajectories with rapid calibration. *Magn Reson Med* 2019;82:1101–1112.

[24] Fessler JA, Lee S, Olafsson VT, Shi HR, Noll DC. Toeplitz-based iterative image reconstruction for MRI with correction for magnetic field inhomogeneity. *IEEE Trans Sig Proc* 2005; 53:3393–3402.

[25] Lustig M, Kim SJ, Pauly JM. A fast method for designing time-optimal gradient waveforms for arbitrary k-space trajectories. *IEEE Trans Med Imag* 2008;27:866–873.

[26] Fessler JA, Sutton BP. Nonuniform fast Fourier transforms using min-max interpolation. *IEEE Trans Sig Proc* 2003;51:560–574.

[27] Yip CY, Fessler JA, Noll DC. Iterative RF pulse design for multidimensional, small-tip-angle selective excitation. *Magn Reson Med* 2005;54:908–917.

[28] Cao Z, Yan X, Grissom WA. Array-compressed parallel transmit pulse design. *Magn Reson Med* 2016;76:1158–1169.

- [29] D. Lee, W. A. Grissom, M. Lustig, A. B. Kerr, P. P. Stang, and J. M. Pauly. VERSE-guided numerical RF pulse design: A fast method for peak RF power control. *Magn Reson Med* 2012; 67:353–362.
- [30] D. Lee, M. Lustig, W. A. Grissom, and J. M. Pauly. Time-optimal design for multidimensional and parallel transmit variable-rate selective excitation. *Magn Reson Med* 2009, 61(6):1471–1479.
- [31] D. Xu, K. F. King, Y. Zhu, G. C. McKinnon, and Z.-P. Liang. Designing multichannel, multidimensional, arbitrary flip angle RF pulses using an optimal control approach. *Magn Reson Med* 2008, 59(3):547–560.
- [32] W. A. Grissom, C. Y. Yip, S. M. Wright, J. A. Fessler, and D. C. Noll. Additive angle method for fast large-tip-angle RF pulse design in parallel excitation. *Magn Reson Med* 2008, 59(4):779–87.

1
2
3
4
5
6
7
8
9
10
11
12
13
14
15
16
17
18
19
20
21
22
23
24
25
26
27
28
29
30
31
32
33
34
35
36
37
38
39
40
41
42
43
44
45
46
47
48
49
50
51
52
53
54
55
56
57
58
59
60

Table Captions

Table 1: W matrix sizes in gigabytes (GB) versus inclusion width in cycles/FOV. An inclusion width of ∞ corresponds to a full matrix solution.

For Peer Review

Figure Captions

Figure 1: (a) A target point \vec{k}_j and the nearby trajectory points that are included when calculating RF pulse weight contributions from this point. Inclusion width is defined as the distance from each target location \vec{k}_j within which all trajectory points are considered when solving for the j -th column of the design (\mathbf{W}) matrix. (b) Calculation of the \mathbf{W} matrix can be performed column-by-column for each target location \vec{k}_j , or patches of target points can be solved for jointly. Here the 16 columns of \mathbf{W} for a 4×4 patch of target points are solved together, and an inclusion width of 4 cycles/FOV dictates that all trajectory points within a 12×12 region centered on the patch are considered in the calculation.

Figure 2: The 24-channel loop Tx array that was simulated in a human head model to obtain B_1^+ maps. The array has diameter 32 cm and height 28 cm. The 16 cm \times 11 cm rectangular loops are arranged in 3 rows of 8.

Figure 3: (a) Middle axial, sagittal, and coronal slices of the target excitation pattern used for all pulse designs. (b) The SPINS trajectory used in the designs. (c) 10 ms minimum-time gradient waveforms that produce the SPINS trajectory.

Figure 4: Normalized excitation patterns (top row) and error maps (bottom row) in central axial, sagittal and coronal slices for k-space domain (left) and spatial domain designs (right).

Figure 5: (a) k-Space computation time versus number of parallel threads, for patch and inclusion widths of 4 cycles/FOV. (b) Computation time (blue axis) and RMSE (red axis) versus patch width, for an inclusion width of 4 cycles/FOV and 16 threads. (c) Computation time (blue axis) and RMSE (red axis) versus inclusion width, for patch widths of 4 and 8 cycles/FOV, and 16 threads.

Figure 6: L-curves for spatial domain and k-space domain pulse designs, repeated across five orders of magnitude of the methods' Tikhonov regularization parameters. The k-space domain designs were repeated using patch and inclusion widths of four versus solving for the entire domain at once ('Patch / Inclusion Widths = 4' versus 'Patch / Inclusion Widths = ∞ '), and using B_1^+ map product interpolation versus phase modulation to each trajectory location ('Interpolated Matrices' versus 'Exact Matrices').

Figure 7: Normalized error maps and RMSEs for (a) pulses designed using a trajectory that reaches 6 mm isotropic resolution and the spatial domain algorithm with a $32 \times 32 \times 24$ grid, (b) pulses designed using the same trajectory and the spatial domain algorithm with a $64 \times 64 \times 48$ grid, and (c) pulses designed using the same trajectory and the k-space domain algorithm with a $32 \times 32 \times 24$ design grid. Red arrows indicate Gibbs ringing in the $32 \times 32 \times 24$ spatial domain design.

Figure 8: Normalized error maps, RMSEs, and computation times for spatial domain design (first row) and k-space domain design (second row), using excitation k-space trajectories with different reduction factors (third row). The reduction factors are referenced to the 10 ms trajectory in Figure 3 (second column).

Figure 9: (a) Normalized off-resonance map containing a Gaussian distortion centered above the frontal sinus, to mimic air-tissue susceptibility difference-induced B_0 inhomogeneity. (b) Normalized excitation maps and RMSEs for spatial domain design with off-resonance correction (first row), and k-space domain design without and with off-resonance correction (second and third rows).

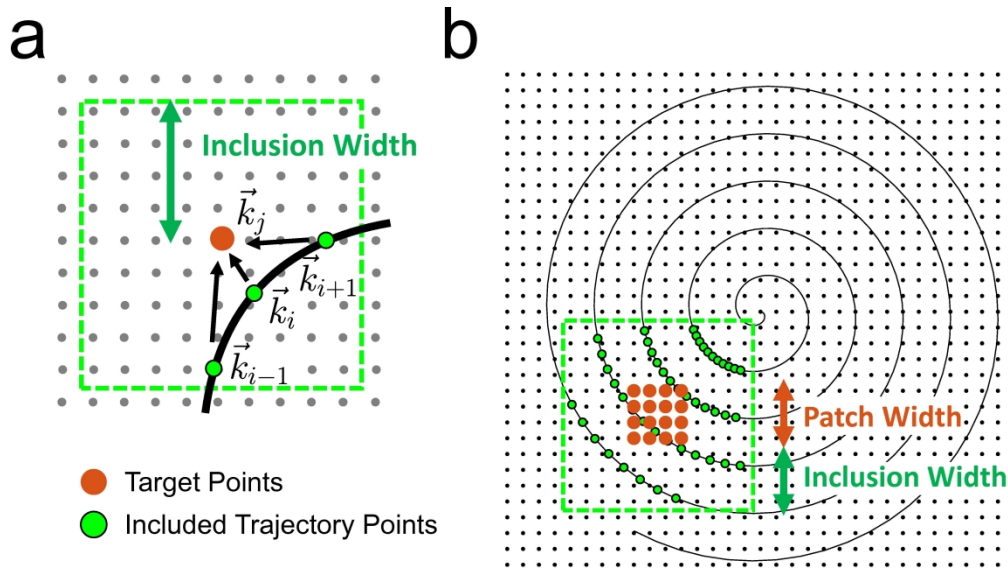


Figure 1: (a) A target point k_j and the nearby trajectory points that are included when calculating RF pulse weight contributions from this point. Inclusion width is defined as the distance from each target location k_j within which all trajectory points are considered when solving for the j -th column of the design (W) matrix. (b) Calculation of the W matrix can be performed column-by-column for each target location k_j , or patches of target points can be solved for jointly. Here the 16 columns of W for a 4×4 patch of target points are solved together, and an inclusion width of 4 cycles/FOV dictates that all trajectory points within a 12×12 region centered on the patch are considered in the calculation.

(Please see main document for caption with intended math typesetting)

197x111mm (600 x 600 DPI)

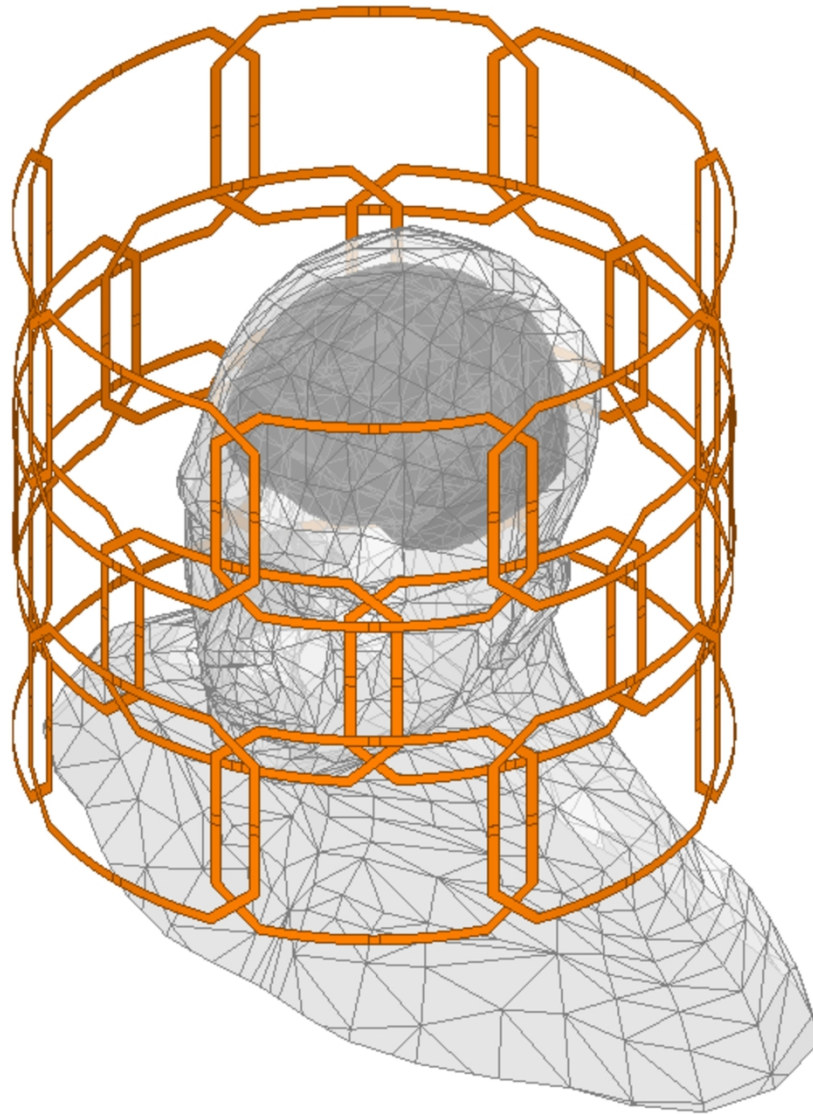


Figure 2: The 24-channel loop Tx array that was simulated in a human head model to obtain B_1^+ maps. The array has diameter 32 cm and height 28 cm. The 16 cm x 11 cm rectangular loops are arranged in 3 rows of 8.

(Please see main document for caption with intended math typesetting)

164x188mm (600 x 600 DPI)

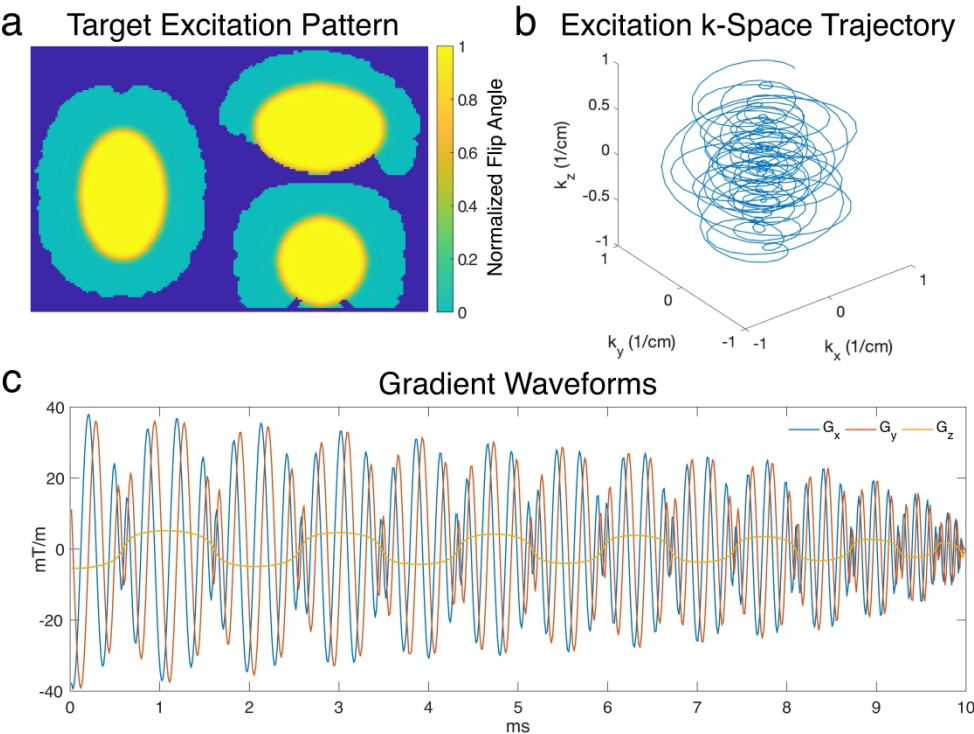


Figure 3: (a) Middle axial, sagittal, and coronal slices of the target excitation pattern used for all pulse designs. (b) The SPINS trajectory used in the designs. (c) 10 ms minimum-time gradient waveforms that produce the SPINS trajectory.

346x258mm (600 x 600 DPI)

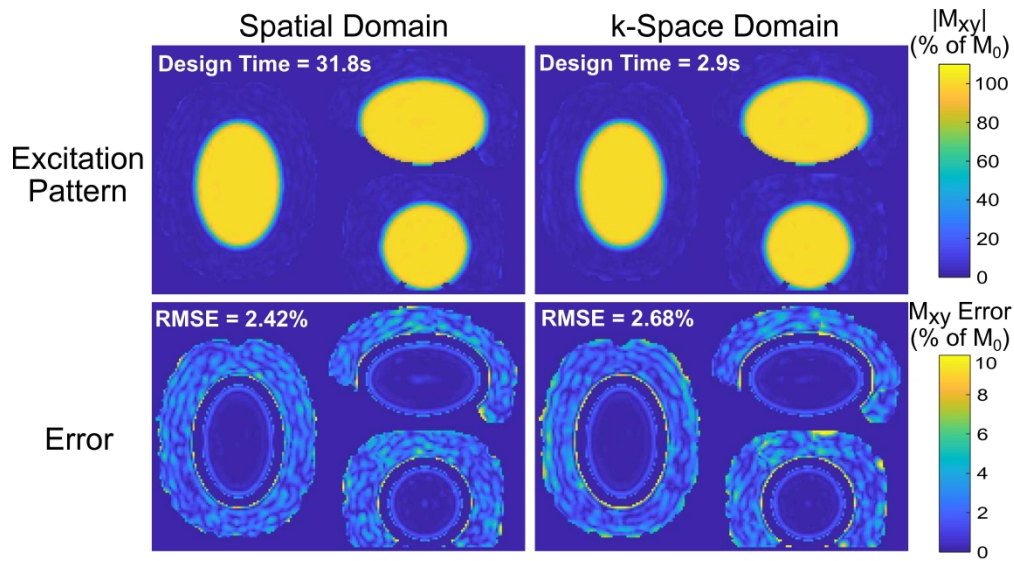


Figure 4: Normalized excitation patterns (top row) and error maps (bottom row) in central axial, sagittal and coronal slices for k-space domain (left) and spatial domain designs (right).

204x112mm (600 x 600 DPI)

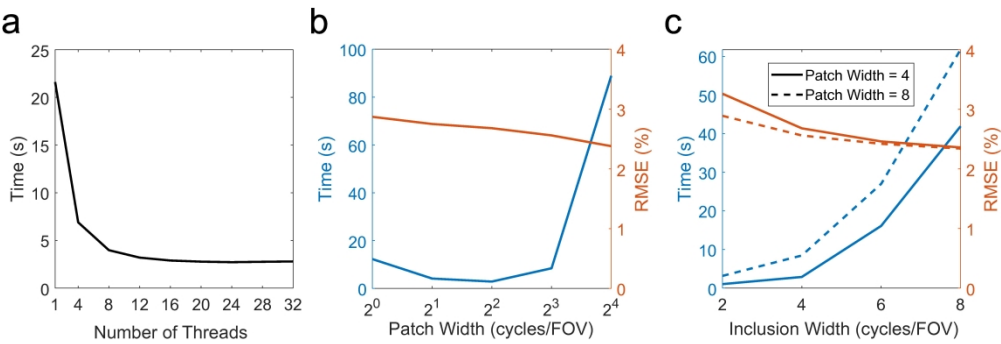


Figure 5: (a) k-Space computation time versus number of parallel threads, for patch and inclusion widths of 4 cycles/FOV. (b) Computation time (blue axis) and RMSE (red axis) versus patch width, for an inclusion width of 4 cycles/FOV and 16 threads. (c) Computation time (blue axis) and RMSE (red axis) versus inclusion width, for patch widths of 4 and 8 cycles/FOV, and 16 threads.

248x82mm (600 x 600 DPI)

Inclusion Width	W Matrix Size (GB)
∞	24.4
8	2.73
6	1.37
4	0.53
2	0.14

Table 1: W matrix sizes in gigabytes (GB) versus inclusion width in cycles/FOV. An inclusion width of infinity corresponds to a full matrix solution. (Please see main document for caption with intended math typesetting)

236x91mm (600 x 600 DPI)

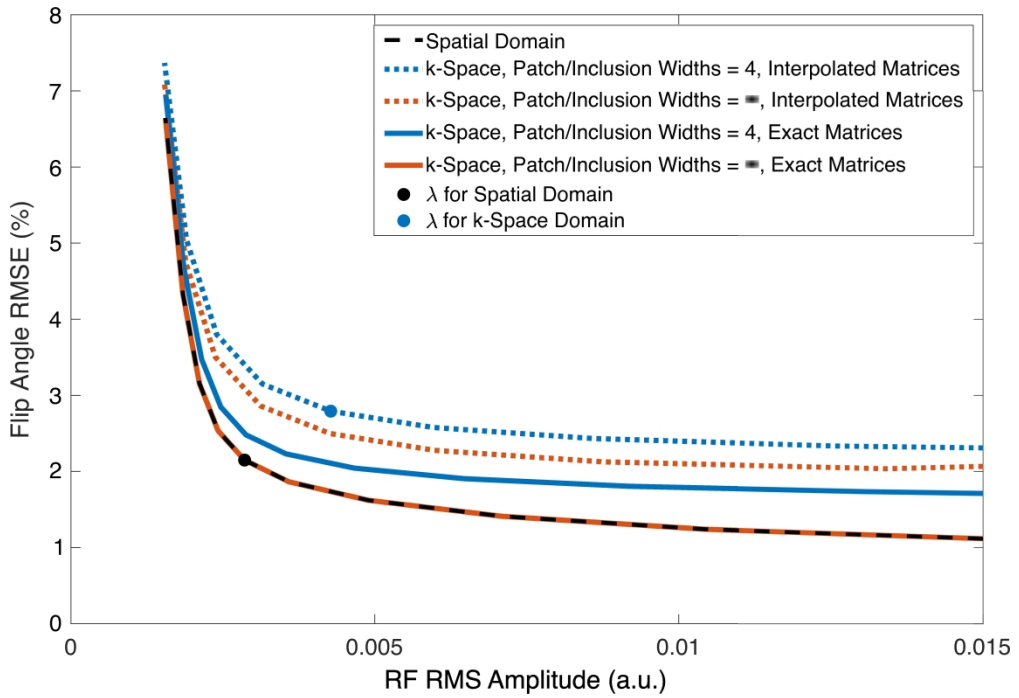


Figure 6: L-curves for spatial domain and k-space domain pulse designs, repeated across five orders of magnitude of the methods' Tikhonov regularization parameters. The k-space domain designs were repeated using patch and inclusion widths of four versus solving for the entire domain at once ('Patch / Inclusion Widths = 4' versus 'Patch / Inclusion Widths = infinity'), and using B1+ map product interpolation versus phase modulation to each trajectory location ('Interpolated Matrices' versus 'Exact Matrices'). (Please see main document for caption with intended math typesetting)

277x190mm (600 x 600 DPI)

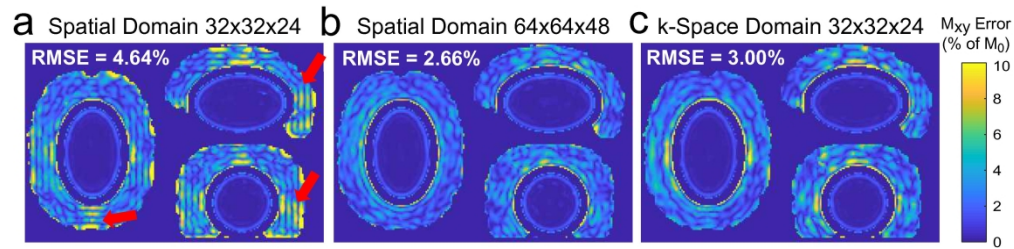


Figure 7: Normalized error maps and RMSEs for (a) pulses designed using a trajectory that reaches 6 mm isotropic resolution and the spatial domain algorithm with a 32x32x24 grid, (b) pulses designed using the same trajectory and the spatial domain algorithm with a 64x64x48 grid, and (c) pulses designed using the same trajectory and the k-space domain algorithm with a 32x32x24 design grid. Red arrows indicate Gibbs ringing in the 32x32x24 spatial domain design. (Please see main document for caption with intended math typesetting)

174x42mm (600 x 600 DPI)

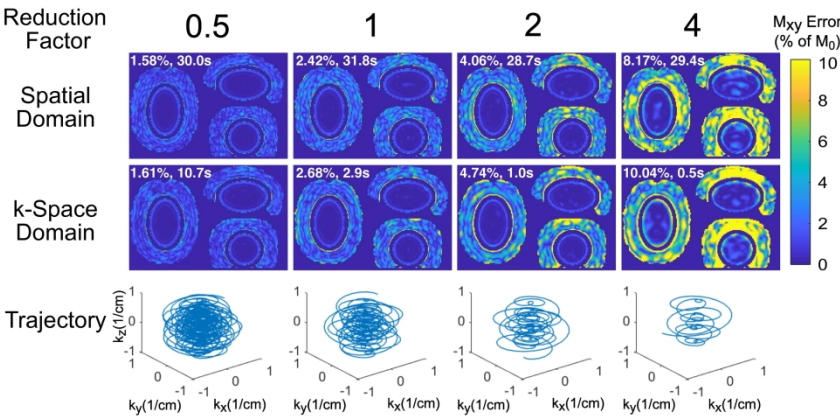


Figure 8: Normalized error maps, RMSEs, and computation times for spatial domain design (first row) and k-space domain design (second row), using excitation k-space trajectories with different reduction factors (third row). The reduction factors are referenced to the 10 ms trajectory in Figure 3 (second column).

305x136mm (300 x 300 DPI)

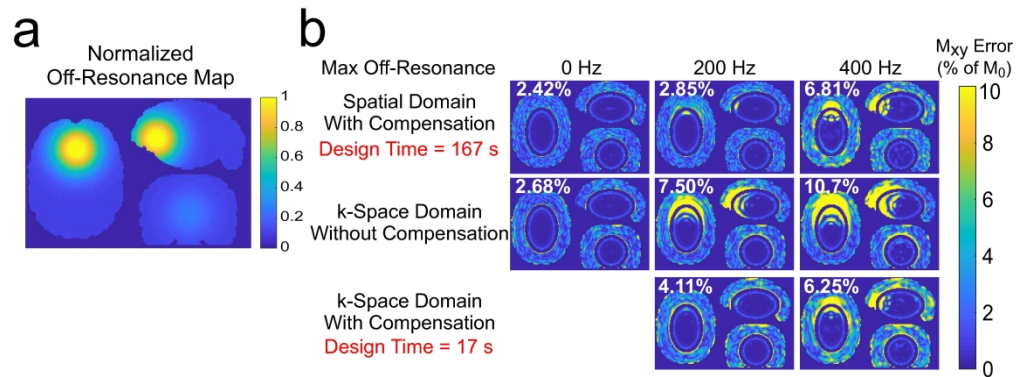


Figure 9: (a) Normalized off-resonance map containing a Gaussian distortion centered above the frontal sinus, to mimic air-tissue susceptibility difference-induced B_0 inhomogeneity. (b) Normalized excitation maps and RMSEs for spatial domain design with off-resonance correction (first row), and k-space domain design without and with off-resonance correction (second and third rows).

233x86mm (600 x 600 DPI)

k-Space Domain Parallel Transmit Pulse Design

Jun Ma^{1,2}, Bernhard Gruber^{3,4}, Xinqiang Yan^{1,5}, and William A. Grissom^{1,2,5*}

October 10, 2020

- ¹Vanderbilt University Institute of Imaging Science, Nashville, TN, United States
- ²Department of Biomedical Engineering, Vanderbilt University, Nashville, TN, United States
- ³A. A. Martinos Center for Biomedical Imaging, Massachusetts General Hospital, Harvard Medical School, Charlestown, MA, United States
- ⁴Division MR Physics, Center for Medical Physics and Biomedical Engineering, Medical University Vienna, Vienna, Austria
- ⁵Department of Radiology and Radiological Sciences, Vanderbilt University, Nashville, TN, United States

Word Count: 5630

*Corresponding author:

Will Grissom

Department of Biomedical Engineering

Vanderbilt University

5824 Stevenson Center

Nashville, TN 37235 USA

E-mail: will.grissom@vanderbilt.edu

Twitter: @wgrissom

Submitted to Magnetic Resonance in Medicine for consideration as a Full Paper.

Acknowledgment: This work was supported by NIH grants R01 EB016695 and U01 EB 025162.

Abstract

Purpose: To accelerate the design of (under- or oversampled) multidimensional parallel transmission pulses. R1.4

Methods: A k-space domain parallel transmission pulse design algorithm was proposed that produces a sparse matrix relating a complex-valued target excitation pattern to the pulses that produce it, and can be finely parallelized. The algorithm was applied in simulations to the design of 3D SPINS pulses for inner volume excitation in the brain at 7 Tesla. It was characterized in terms of the dependence of computation time, excitation error, and required memory on algorithm parameters, and it was compared to the spatial domain pulse design method in terms computation time, excitation error, Gibbs ringing, and ability to compensate off-resonance. R1.1

Results: The proposed algorithm achieved approximately 90% faster pulse design compared to an iterative spatial domain method, with the same number of parallel threads, with the tradeoff of increased excitation error and RMS RF amplitude. It reduced the memory required to store the design matrix by 98% compared to a full matrix solution. Even with a coarse design grid, the algorithm produced patterns that were free of Gibbs ringing. It was similarly sensitive to k-space undersampling as the spatial domain method, and was similarly capable of compensating for off-resonance.

Conclusion: The proposed k-space domain algorithm accelerates and finely parallelizes parallel transmission pulse design, with a modest tradeoff of excitation error and RMS RF amplitude.

Key words: Parallel Transmission; RF pulses; Ultra-high field MRI; RF pulse design; Selective excitation.

Introduction

Multidimensional parallel transmission [1, 2] has been widely investigated for applications including reduced field-of-view imaging [3, 4], transmit field (B_1^+) inhomogeneity compensation [5, 6], and compensation of susceptibility-induced signal loss [7]. One of the first small-tip-angle pulse design algorithms developed to demonstrate the concept of parallel transmission was formulated in the excitation k-space domain [1]. In that method, a dense system matrix was constructed by applying a Fourier transform to each transmit coil's B_1^+ map, forming a convolution matrix for each coil, and then concatenating the coils' convolution matrices. The pulses were solved by multiplying the regularized pseudoinverse of the system matrix into the target excitation pattern's Fourier transform. A spatial domain small-tip-angle parallel transmit pulse design algorithm [8] was proposed soon after, wherein a non-uniform discrete Fourier transform matrix is constructed, duplicated for each transmit coil, and weighted by that coil's B_1^+ map. The weighted matrices are concatenated and the pulses are solved by regularized pseudoinverse of the system matrix or using an iterative method. The spatial domain method is mathematically straightforward and enables flexible modeling and compensation of effects such as off-resonance, and incorporation of regions of interest. Since its introduction, most small-tip-angle parallel transmission studies have been formulated in the spatial domain [9, 10].

R2.2

Despite the advantages of the spatial domain approach, it can have prohibitive computational requirements when the number of coils and the number of dimensions become large, for example in three-dimensional [11, 12] or spectral-spatial pulse designs [13–16], when there is a large number of coils [17], and when off-resonance compensation is used. The spatial domain system matrix typically has dimensions $N_s \times (N_c \cdot N_t)$, where N_s is the number of spatial and spectral locations defined in the target excitation pattern, N_c is the number of transmit channels, and N_t is the number of time points in the pulse. Typical values for N_s range from 1,000 for 2D designs to 250,000 for 3D designs, the number of coils varies from 8 to 32 on ultra-high field scanners, and the number of time points varies from 500 to 2,500. Overall, for a 3D design the spatial domain system matrix can occupy upwards of 120 gigabytes of memory, making it infeasible to construct and invert on most

computers. Explicit matrix storage and inversion can be avoided using non-uniform fast Fourier transforms (NUFFTs) to evaluate matrix multiplies, combined with iterative conjugate gradient solvers. In such designs, parallelization can be applied across coils, and GPU-based pulse designs have been described [18]. However, parallelization cannot be applied across iterations; several tens of iterations are commonly used for 3D designs and thousands of iterations can be required for magnitude least-squares [19] or constrained pulse designs [20, 21]. A further challenge for parallel transmit pulse design is that pulses must be computed for each subject, as a pre-scan stage while the subject lies in the scanner.

R2.1

Here we describe a single-step (non-iterative) small-tip-angle excitation k-space-domain pulse design algorithm with low memory requirements, that can be applied to large pulse design problems with fine parallelization. The algorithm produces a sparse k-space-domain pseudoinverse pulse design matrix that directly relates the Fourier transform of a complex-valued target excitation pattern to the RF pulses that produce it. Once the matrix is built, RF pulses are instantaneously solved by a sparse matrix multiplication, and the matrix need not be recomputed if the target pattern changes. The algorithm takes advantage of the compactness of B_1^+ maps in excitation k-space to independently formulate and solve a parallelizable set of small matrix-vector subproblems to obtain the significant entries of each column or groups of columns of the sparse design matrix.

R1.1

In the following, we derive the independent solution for each column of the design matrix and introduce a patch-wise parallelization that provides control over the size and accuracy of each subproblem. We describe an efficient method to construct a required matrix of B_1^+ map inner products while maintaining accuracy. A method to incorporate off-resonance correction is also described. The algorithm was characterized and validated in terms of excitation error and computation time, with comparisons to spatial domain designs using NUFFTs and the conjugate gradient algorithm. The application for the designs was a three-dimensional inner-volume excitation using a simulated 24-channel transmit array and a SPINS trajectory [11]. An early account of this work was provided in Ref. [22].

Theory

k-Space-Domain Subproblems

We propose to compute a sparse design matrix \mathbf{W} that directly maps the Fourier transform of a desired spatial excitation pattern to a vector of RF pulses that together produce the pattern, as:

$$\mathbf{b} = \mathbf{W}\mathcal{F}(\mathbf{d}), \quad [1]$$

where \mathbf{b} is a vector of concatenated multi-channel RF pulses with length $N_t N_c$, where N_t and N_c are the numbers of time points and channels, respectively, and $\mathcal{F}(\mathbf{d})$ is a length- N_s vector containing the Fourier transform of the **complex-valued** target k-space excitation pattern \mathbf{d} . \mathbf{W} has dimensions $N_t N_c \times N_s$. Once the entries of \mathbf{W} are computed, the RF design problem can be instantaneously solved by a sparse matrix multiplication. Here we describe how to break down the problem of constructing \mathbf{W} into a set of smaller independent subproblems that can be solved in parallel.

R1.1

The columns of \mathbf{W} can be solved independently, based on the observation that if the desired k-space pattern is a delta function at a k-space location \vec{k}_j ($1 \leq j \leq N_s$), then only the j -th column \mathbf{w}_j of \mathbf{W} is required to relate the desired k-space pattern to the desired RF pulse. In this case, the vector \mathbf{w}_j is identical to the desired RF. Therefore, the problem of finding the j -th column \mathbf{w}_j of \mathbf{W} can be stated as: what should the RF pulse samples be to generate a unit delta function at the location \vec{k}_j in k-space, and zeros elsewhere? Mathematically, the relationship that should be satisfied by the weights in column \mathbf{w}_j can be expressed as:

$$\delta(\vec{k} - \vec{k}_j) = \sum_{i=1}^{N_t} \sum_{c=1}^{N_c} w_c(\vec{k}_i) s_c(\vec{k} - \vec{k}_i), \quad [2]$$

where i indexes time points in the pulses' excitation k-space trajectory, and c indexes channels. $w_c(\vec{k}_i)$ is the $((c-1)N_t + i)$ -th element of the \mathbf{w}_j vector, and $s_c(\vec{k} - \vec{k}_i)$ is the Fourier transform of channel- c 's B_1^+ map, shifted to be centered at excitation k-space location \vec{k}_i . Equation 2 can be restated in matrix-vector form as:

$$\mathbf{S}\mathbf{w}_j = \delta_j, \quad [3]$$

where \mathbf{S} is a $N_s \times N_c N_t$ matrix containing values of $s_c(\vec{k} - \vec{k}_i)$ for all c and i , and δ_j is a vector containing a one in the entry corresponding to excitation k-space location \vec{k}_j , and zeros in all other entries. The regularized pseudoinverse solution for w_j is:

$$w_j = (\mathbf{S}^H \mathbf{S} + \lambda \mathbf{I})^{-1} s_j^H \quad [4]$$

where s_j^H is the conjugate transpose of the j -th row of \mathbf{S} .

If all points on the excitation k-space trajectory are considered in Equation 2, then there is no reduction in computation compared to a conventional pseudoinverse-based pulse design. However, because B_1^+ maps are localized near $\vec{k} = 0$ in excitation k-space, only a small number ($\ll N_t$) of trajectory points near the target location \vec{k}_j can contribute significantly to the excitation pattern at \vec{k}_j or its neighbors, and therefore need to be considered in the subproblem; all other trajectory points can be ignored. This means Equation 2 can be modified to:

$$\delta(\vec{k} - \vec{k}_j) = \sum_{\vec{k}_i \in \mathbb{N}} \sum_{c=1}^{N_c} w_c(\vec{k}_i) s_c(\vec{k} - \vec{k}_i), \quad [5]$$

where \mathbb{N} is the set of trajectory points in the vicinity of \vec{k}_j . In this work ‘inclusion width’ is defined as the distance, in [phase cycles over the excitation field-of-view \(cycles/FOV\)](#), from each target location \vec{k}_j within which all trajectory points are accrued into \mathbb{N} . This reduced set of trajectory points reduces the column dimension of \mathbf{S} and both dimensions of $\mathbf{S}^H \mathbf{S}$, and implies that the design matrix \mathbf{W} is sparse. Figure 1a illustrates a target point \vec{k}_j for a two-dimensional pulse design, and the nearby points on the trajectory that need to be included in the solution for w_j for an inclusion width of 4 cycles/FOV. R1.2

The \mathbf{W} matrix columns w_j can be solved in parallel one-at-a-time or patch-wise, wherein all target points in a patch share the same $\mathbf{S}^H \mathbf{S}$ matrix, and their s_j^H vectors are concatenated in the column dimension to form a matrix in Equation 4. An illustration of a 4×4 patch and its included trajectory points is shown in Figure 1b, for a two-dimensional spiral pulse design. The inclusion width is also 4 cycles/FOV from any target point in the patch, so all the excitation trajectory points within a 12×12 cycles/FOV square are included in the calculation.

Efficient $\mathbf{S}^H \mathbf{S}$ matrix construction

Constructing the $\mathbf{S}^H \mathbf{S}$ matrix by first constructing \mathbf{S} is computationally expensive because it requires each channel's B_1^+ map to be shifted to each trajectory location \vec{k}_i by phase modulation followed by Fourier transform, or by Fourier transform followed by interpolation. Furthermore, the matrix multiplication between \mathbf{S}^H and \mathbf{S} is also computationally intensive due to the potentially large row dimension of \mathbf{S} , if the zero excitation condition is enforced on a large grid of points around each \vec{k}_j . The computational costs can be reduced by truncating the B_1^+ maps in k-space, but this introduces large errors. Instead, inspired by the non-Cartesian GRAPPA method of Ref [23], we propose to construct the Hermitian $\mathbf{S}^H \mathbf{S}$ matrix directly via interpolation of the Fourier transforms of inner products of pairs of B_1^+ maps. The $\mathbf{S}^H \mathbf{S}$ matrix can be written in block form as:

$$\mathbf{S}^H \mathbf{S} = \begin{pmatrix} \mathbf{S}_1^H \mathbf{S}_1 & \cdots & \mathbf{S}_1^H \mathbf{S}_{N_c} \\ \vdots & \ddots & \vdots \\ \mathbf{S}_{N_c}^H \mathbf{S}_1 & \cdots & \mathbf{S}_{N_c}^H \mathbf{S}_{N_c} \end{pmatrix}, \quad [6]$$

where each sub-matrix $\mathbf{S}_i^H \mathbf{S}_j$ contains inner products of the Fourier transforms of channel i and channel j 's B_1^+ maps, after they are shifted to be centered different points on the excitation trajectory corresponding to the row and column indices of the sub-matrix. These inner products can be calculated by interpolating the Fourier transform of the inner product of channel i and channel j 's B_1^+ maps. In other words, each element in the Hermitian matrix $\mathbf{S}_i^H \mathbf{S}_j$ is the vector sum of channel i and channel j 's shifted k-space B_1^+ maps, which is also a single point of their k-space convolution. Via the multiplication property of the Fourier transform, this convolution in k-space can be calculated from the Fourier transform of the dot product of the two spatial domain B_1^+ maps. For further details, please refer to Ref. [23].

Since $\mathbf{S}^H \mathbf{S}$ and its sub-matrices are Hermitian, we only need to find the values within the lower triangle of the matrix, which are the sub-matrices $\mathbf{S}_i^H \mathbf{S}_j$ with $i > j$ that are themselves lower triangular. The elements of a given sub-matrix $\mathbf{S}_i^H \mathbf{S}_j$ are interpolated from a densely sampled Fourier transform of the dot product of the spatial domain B_1^+ maps of the i -th and j -th channels. The

(m, n) -th element is the value interpolated at a position $\vec{k}_m - \vec{k}_n$ away from DC, where \vec{k}_m and \vec{k}_n are the excitation k-space trajectory locations corresponding to row m and column n . Compared to phase-modulating and Fourier transforming each channel's B_1^+ map for each point on the trajectory which would require $N_t N_c$ Fourier transforms, to solve all the columns of \mathbf{W} the total number of Fourier transforms needed in this efficient method is $N_c(N_c + 1)/2$. The storage size is also much smaller, and the matrix multiplication between \mathbf{S}^H and \mathbf{S} is avoided.

Off-Resonance Compensation

Off-resonance compensation is common in spatial-domain parallel pulse designs [8], but has not been previously implemented in a k-space-domain design. Spatial domain designs based on NUFFTs make use of an approximate time-segmented model for the off-resonance term [24], which decouples the space- and time-dependence of off-resonant phase accrual into the product of space- and time-dependent terms, which are applied on either side of the NUFFT operator. Here we show how a time-segmented off-resonance model can be incorporated in the proposed k-space-domain algorithm. Mathematically, the time-segmented model is given by:

$$e^{i\Delta\omega(\vec{x}_j)(t_i-T)} \approx \sum_{l=1}^L b_l(t_i) h_l(\vec{x}_j), \quad [7]$$

where $\Delta\omega(\vec{x}_j)$ is the off-resonance frequency at \vec{x}_j , i indexes time points in the pulse, T is the pulse duration, and l indexes the L time segments, where L is typically between 4 and 8. The $b_l(t_i)$ functions are temporal interpolators that multiply into the RF samples and are determined by numerical optimization as described in Ref. [24], and $h_l(\vec{x}_j) = e^{i\Delta\omega(\vec{x}_j)\check{t}_l}$ are the off-resonance phase shifts applied to the excitation patterns produced by the RF pulse time segments centered at time points $\{\check{t}_l : l = 1, \dots, L\}$. The time-segmented off-resonance model can be incorporated into Equation 2 as:

$$\delta(\vec{k} - \vec{k}_j) = \sum_{l=1}^L \sum_{i=1}^{N_t} \sum_{c=1}^{N_c} w_c(\vec{k}_i) b_l(t_i) \tilde{s}_{cl}(\vec{k} - \vec{k}_i), \quad [8]$$

where $\tilde{s}_{cl}(\vec{k})$ is the Fourier transform of the product of channel c 's B_1^+ map and time segment l 's off-resonance phase shift $h_l(\vec{x}_j)$. We can then write the equivalent of Equation 3 with the off-

resonance model:

$$\sum_{l=1}^L \mathbf{S}_l \text{diag}(b_l(t_i)) \mathbf{w}_j = \delta_j, \quad [9]$$

where the matrix \mathbf{S}_l is now formed from the $N_c L$ Fourier transforms of the B_1^+ map and $h_l(\vec{x}_j)$ products. Efficient construction of the $\mathbf{S}^H \mathbf{S}$ matrix follows much the same procedure as without off-resonance except that with off-resonance, the elements of each sub-matrix $\mathbf{S}_i^H \mathbf{S}_j$ in Equation 6 are interpolated from $L(L+1)/2$ Fourier transformed maps, and the interpolated values are weighted by the temporal interpolators for each pair of multiplied time segments before they are summed. Compared to constructing $\mathbf{S}^H \mathbf{S}$ without off-resonance, taking off-resonance into account increases the total number of FFT operations from $N_c(N_c+1)/2$ to $N_c L(N_c L+1)/2$, and increases the number of interpolations needed for each sub-matrix element from 1 to $L(L+1)/2$. However, we note that only adjacent time segments with overlapping temporal interpolators at a given time point need to be considered when calculating the elements of $\mathbf{S}^H \mathbf{S}$ corresponding to that time point.

R1.3

Methods

Design and Simulation Setup

Simulations were performed to validate and characterize the proposed k-space domain parallel transmit pulse design method, with comparisons to a least-squares spatial-domain design [8]. RF pulses were designed for a simulated 24-channel loop transmit array (Figure 2) that is being built for a 7 Tesla scanner optimized for imaging the human cortex. 24-channel complex-valued B_1^+ maps used in the pulse designs were simulated in a male human head model using Ansys High Frequency Structure Simulator (Canonsburg, PA, USA) with 1.5 mm isotropic resolution. Figure 3a shows the target pattern for all pulse designs which comprised an ellipse centered on the ventricles with AP/HF/LR semi-axes of 4.8/3.2/3.2 cm, with zero phase. The pattern was smoothed by a Fermi filter that was applied in the frequency domain to match the target pattern's effective resolution to the excitation k-space trajectory's 5 mm resolution. This choice of target pattern was motivated

R1.1

by imaging applications for the 7 Tesla scanner in which midbrain signals will be saturated for high-resolution, highly-accelerated imaging of the cortex. Pulses were designed to excite the entire ellipse and achieve zero excitation in voxels in the cerebrum but outside the ellipse. The smoothed target pattern and the B_1^+ maps were downsampled from their original $128 \times 128 \times 96$ grids (1.5 mm isotropic resolution) to $64 \times 64 \times 48$ grids (3 mm isotropic resolution), and RF designs were performed with the $64 \times 64 \times 48$ grid size.

A SPINS excitation k-space trajectory [11] (Figure 3b) with 5 mm max resolution was used for the designs. The SPINS trajectory comprised three segments with radii ranging between 1-0.625, 0.625-0.375, and 0.375-0 cycles/cm, respectively. The number of polar and azimuthal rotations were 15.5/2.125, 20.66/2.833, 15.5/2.125 for each segment, respectively. The SPINS trajectories were first designed analytically and the final gradient waveforms and excitation k-space trajectories were designed from them using the minimum-time gradient waveform design method [25], for a 15 μ s dwell time and subject to the scanner's gradient amplitude and slew rate constraints of 200 mT/m and 700 T/m/s, respectively (Figure 3c). The durations of the three segments after minimum-time gradient design were 4.174, 4.326, and 1.5 ms, respectively. With the exception of the simulations across undersampling factors, all pulse designs used this 10 ms trajectory. With this trajectory and the $64 \times 64 \times 48$ design grid size, the dimensions of the \mathbf{W} matrix were 16,632 RF pulse samples, by 196,608 target k-space locations.

All pulse designs and Bloch equation simulations were performed in MATLAB (Mathworks, Natick, MA, USA). For spatial domain designs, RF pulses were solved using an iterative least-squares conjugate-gradient descent method with 35 iterations, which was accelerated by NUFFTs [26]. Except for the off-resonance-compensated designs described below, all spatial domain designs were parallelized using 16 threads that simultaneously computed the forward and backward NUFFTs across transmit coils. The proposed k-space domain algorithm was implemented based on code for the non-Cartesian GRAPPA method of Ref. [23], as a function that takes as input the B_1^+ maps and a normalized excitation k-space trajectory. Within that function the Fourier transforms of the B_1^+ products are calculated, and a C-based [MATLAB Executable \(MEX\)](#) function

R1.6

is invoked to solve for the non-zero elements of each column of \mathbf{W} , with linear interpolation of the Fourier transforms of the B_1^+ map products to obtain the entries of the $\mathbf{S}^H \mathbf{S}$ matrices. Those elements are then inserted into a sparse \mathbf{W} matrix, which is the single output of the main function. Parallelization was implemented across patches within the C-based MEX function using the [Open Multi-Processing \(OpenMP\)](#) library. The final pulses are calculated by multiplying the sparse \mathbf{W} matrix into the Fourier transform of the target pattern. This code, the B_1^+ maps, and a demo script are available at <https://github.com/wgrissom/kpTx>. All pulse designs were performed on a server (Colfax International, Santa Clara, CA, USA) with 512 GB RAM and two 24-core 2.1 GHz Intel Xeon CPUs which provide up to 94 threads (Intel Corporation, Santa Clara, CA, USA). Designs were performed five times for each case, and the mean computation time was recorded. For the k-space domain designs, the design time comprised the time to compute the sparse \mathbf{W} matrix, and the time to multiply it into the target pattern to obtain the pulses. The resulting pulses were Bloch equation-simulated and compared to the target pattern on the finer $128 \times 128 \times 96$ grid to capture Gibbs ringing. When calculating excitation errors, the magnitude root-mean-square error (RMSE) was calculated in voxels within the cerebrum, except for an ≈ 5 mm-thick transition band around the edge of the elliptical target region.

R1.6

k-Space Algorithm Parameters

To evaluate how accuracy and compute time depend on k-space-domain design parameters and parallelization, pulse designs were done across numbers of threads (i.e., how many patches were solved simultaneously; 1 to 32), patch widths (1 to 16 cycles/FOV), and inclusion widths (2 to 8 cycles/FOV). The number of threads were varied while holding the patch width and inclusion width both at 4 cycles/FOV. The patch width was varied while holding the number of threads at 16, and the inclusion width at 4 cycles/FOV, and the inclusion width was varied (2, 4, 6, and 8 cycles/FOV) while holding the number of threads at 16, and the patch width at 4 and 8 cycles/FOV. The sizes of the \mathbf{W} matrices were also recorded, holding patch width constant at 4 cycles/FOV and varying the inclusion width.

L-Curves

To compare the tradeoff between excitation error (measured by root-mean-square error) and integrated RF root-mean-square (RMS) amplitude for spatial and k-space domain designs, pulse designs were repeated while varying Tikhonov regularization parameters (λ in Equation 4) over five orders of magnitude. The k-space domain designs were repeated four times to investigate the two main sources of error: finite patch and inclusion widths, and B_1^+ map product interpolation when building the $S^H S$ matrices. Specifically, for each λ a design was performed using patch and inclusion widths of four ('Patch/Inclusion Widths = 4') with interpolated B_1^+ map products ('Interpolated Matrices'), patch and inclusion widths covering the entire design grid ('Patch/Inclusion Widths = ∞ ') with interpolated B_1^+ map products, patch and inclusion widths of four without B_1^+ map product interpolation ('Exact Matrices'; B_1^+ maps were phase-modulated to each trajectory location before Fourier transform), and patch and inclusion widths covering the entire design grid without B_1^+ map product interpolation. Note that the last case is equivalent to the original k-space domain method of Ref. [1]. For each design, flip angle RMSE (calculated using the spatial domain NUFFT) and root-mean-square RF amplitude were recorded.

Gibbs Ringing

Gibbs ringing commonly arises in spatial domain parallel pulse designs when the resolution of the design grid is similar to that of the excitation k-space trajectory. The proposed k-space-domain method is implemented without wraparound or circulant end conditions in excitation k-space, so Gibbs ringing should be suppressed even when using a design grid that is only slightly wider than the trajectory. To demonstrate this, the target pattern and B_1^+ maps were further down-sampled to $32 \times 32 \times 24$ (6 mm isotropic-resolution), and the outermost leaves of the SPINS trajectory which had duration 2.1 ms were excluded so that the maximum excitation resolution matched the 6 mm target pattern and B_1^+ map resolution. Using this shorter 7.9 ms trajectory, pulses were designed by the spatial domain method using both $32 \times 32 \times 24$ and $64 \times 64 \times 48$ grid sizes, and by the k-space-domain method for $32 \times 32 \times 24$ grid size. The Tikhonov regularization parameters for the

32×32×24 designs were set so that the RMS RF amplitudes produced by the k-space domain and spatial domain designs matched. The designed pulses were then evaluated against the target pattern using the 128×128×96 grid size, to visualize the ringing.

Excitation k-Space Undersampling

An important application of parallel transmission is the reduction of multidimensional pulse durations by excitation k-space undersampling. To compare the spatial domain and k-space domain methods across undersampling factors, the number of polar and azimuthal rotations in each segment of the SPINS trajectory were increased and reduced relative to the reference design described above, by factors of 0.5, 2, and 4. That is, for a reduction factor of 0.5, the number of polar and azimuthal rotations in the trajectory were doubled for each of the three segments, and they were halved for a reduction factor of 2. This yielded pulse durations of 20.5 ms (reduction factor 0.5), 5.3 ms (reduction factor 2), and 2.6 ms (reduction factor 4).

R2.1

Off-Resonance

To compare the off-resonance-compensated k-space domain designs with off-resonance-compensated spatial domain designs, we incorporated a Gaussian ($\sigma = 3$ cm) field map centered above the frontal sinus, which was designed to mimic the characteristic susceptibility-induced B_0 inhomogeneity in this part of the human brain. The field maps were then scaled so that the maximum off-resonance reached +200 Hz and +400 Hz. A time-segmented approximate off-resonance model was calculated using the method of Ref. [24] with $L = 4$ time segments, and this model was used in both spatial domain and k-space domain designs. Both spatial domain and k-space domain designs used 32 parallel threads.

Results

Figure 4 shows simulated excitation patterns and error maps for the reference spatial and k-space domain designs. Both designs were performed with 16 parallel threads and the $64 \times 64 \times 48$ grid size (3 mm isotropic resolution), and the excitation patterns were evaluated against the target pattern on a $128 \times 128 \times 96$ grid size (1.5 mm iso-resolution). The k-space domain design used patch and inclusion widths of 4. The calculated root-mean-squared errors (RMSEs) were 2.42% (spatial domain) and 2.68% (k-space domain), respectively. For both design methods, most of the errors appeared at the edges of the transition band, and errors elsewhere were lower than 5% of the target flip angle. This indicates uniform inner volume excitation while maintaining the outer volume intact. The parallelized k-space domain design required 2.9 seconds computation versus 31.8 seconds for the spatial domain method, a 91% decrease.

k-Space Algorithm Parameters

Figure 5a plots mean computation time versus number of parallel threads, holding the patch and inclusion widths fixed at 4 cycles/FOV. The computation time decreased rapidly with increasing thread number up to 12 threads, and then plateaued, likely due to the overhead involved in initiating threads after that point. Based on this result, the number of threads was held fixed at 16 for subsequent designs when off-resonance was not compensated.

Figure 5b plots mean computation time and RMSE with different patch widths. The computation time decreased up to a patch width of 4 cycles/FOV (corresponding to $4^3 = 64$ simultaneously solved columns of \mathbf{W}) and then increased sharply for larger patch widths. RMSE decreased slowly as the patch width increased since the number of excitation trajectory points included in the calculation of weights for each target point increases on average (and especially for target locations in the middle of each patch) as the patch width increases, even when the inclusion width stays fixed. Based on this result, a patch width of 4 cycles/FOV was used for subsequent designs.

Figure 5c plots mean computation time and RMSE with different inclusion widths. The solid lines and dashed lines were obtained with patch widths of 4 and 8 cycles/FOV, respectively. Com-

putation time increased and error decreased with increasing inclusion width, since more excitation trajectory points were included in each target location’s calculation for increasing inclusion width, corresponding to an increased $S^H S$ matrix size. The RMSE was only slightly lower for a patch width of 8 versus 4 cycles/FOV, but the computation time was much higher for 8 cycles/FOV, across all inclusion widths. The knees in the curves occurred approximately at an inclusion width of 4 cycles/FOV, so this value was used in subsequent designs.

Table 1 lists the size of the final matrix W in gigabytes, versus inclusion width. As inclusion width increases, more excitation trajectory points are used in the solution of the weights for each target location, until the entire trajectory is used for each location (inclusion width = ∞ in the table), corresponding to a full solution. With the inclusion width of 4 cycles/FOV used here, the matrix size was 98% smaller than that of a full solution.

L-Curves

Figure 6 plots flip angle RMSE versus RF RMS amplitude for the spatial domain method and different configurations of the k-space domain method. The spatial domain method achieves the best overall tradeoff between error and RMS amplitude (dashed black curve), which is matched by the k-space domain method when all target locations are solved simultaneously with all excitation trajectory points included and exact $S^H S$ matrix construction (orange curve). When the inclusion and patch widths are limited to 4 cycles/FOV but the $S^H S$ matrices are still constructed exactly, there is an increase in error and RMS amplitude (solid blue curve). However, a larger penalty is incurred by interpolating the entries of the $S^H S$ matrices (dashed orange curve) than by limiting the inclusion and patch widths. Combining interpolation of the $S^H S$ matrix entries and patch and inclusion widths of 4 cycles/FOV yield the dashed blue curve, which has a higher error and RF amplitude than when interpolation or small patch and inclusion widths are used alone. Overall, these results and the results in Figure 5 and Table 1 show that the k-space domain method allows a tradeoff between computation time and memory usage versus excitation error and RMS RF amplitude. The dots on the spatial domain and k-space domain curves indicate the knees of the

R1.9

curves corresponding to the λ values used for the designs in Figures 4, 5, 8, and 9. Note that the RMSE's in Figure 6 are slightly lower for the spatial domain designs and slightly higher for the k-space domain designs compared to other figures, because the flip angle errors in Figure 6 were calculated using spatial domain NUFFTs instead of Bloch equation simulations, to provide a more direct measure of the design error.

Gibbs Ringing

Figure 7a shows slices of the excitation error pattern produced by pulses designed by the spatial domain method on a $32 \times 32 \times 24$ grid, which were Bloch-simulated on the original $128 \times 128 \times 96$ grid. There is significant Gibbs ringing in the pattern (indicated by the red arrows), and the pulses incur a higher RMSE (4.64%) than pulses designed using either the spatial domain method with a finer $64 \times 64 \times 48$ grid (2.66%; Figure 7b) or the k-space domain method with a $32 \times 32 \times 24$ grid (3.00%; Figure 7c). Gibbs ringing is not apparent in either the $64 \times 64 \times 48$ spatial domain error pattern or the $32 \times 32 \times 24$ k-space domain error pattern. The RMS RF amplitudes of the low-resolution designs were both 0.005. Note that the error of the $64 \times 64 \times 48$ spatial domain design is slightly higher than designs presented in other figures due to the lower-resolution excitation trajectory. From a spatial domain point of view, the Gibbs ringing in the low-resolution spatial domain design was caused by the design's inability to observe and limit the ringing in the low-resolution design grid. From a k-space domain point of view, the Gibbs ringing was due to implicit circulant end conditions at the edges of excitation k-space, which led RF samples at one edge of k-space to wrap-around and affect target locations at the opposite edge of k-space. This effect is mitigated using a high-resolution spatial domain design grid, as illustrated in Figure 7b. However, even for a low-resolution k-space domain design there is no wrap-around effect in excitation k-space because the trajectory points that are incorporated in solution for each patch are explicitly specified to be those in the immediate vicinity of that patch, without circulant end conditions.

Excitation k-Space Undersampling

Figure 8 compares excitation error patterns produced by spatial domain-designed pulses (top row) and k-space domain-designed pulses (middle row), for different trajectory reduction factors which resulted in the SPINS trajectories plotted in the third row. For each design the k-space domain-designed pulses had higher error, but error increased smoothly with increasing reduction factor, as it did for the spatial domain designs. Figure 8 also reports mean computation time for each design. The spatial domain times were fairly constant across reduction factors despite the decreasing number of time samples with increasing reduction factor. This was because the size of the FFT operations in the NUFFTs depended not on the length of the trajectory but on the size of the target pattern which did not change with reduction factor, and the FFT operations dominated the NUFFT computation times relative to the gridding operations. Conversely, the k-space domain times did decrease with reduction factor since the number and sizes of the $S^H S$ matrices depend on the trajectory length.

R2.1

Off-Resonance

Figure 9a shows the off-resonance maps containing a Gaussian distortion which was centered above the frontal sinus, and scaled to peak amplitudes of 0, 200, and 400 Hz for the pulse designs and Bloch simulations. Figure 9b shows excitation error patterns and RMSEs for spatial domain designs with off-resonance compensation, and k-space domain designs without and with off-resonance compensation. Without off-resonance compensation, the k-space domain-designed pulses produced large ($> 10\%$ of M_0) excitation errors both inside and outside the target ellipse. When the off-resonance map was incorporated in the spatial domain and k-space domain designs, the distortion was nearly fully corrected when it had a peak amplitude of 200 Hz. When the map was scaled to a peak of 400 Hz, some large errors remained, with the k-space domain-designed pulses achieving slightly lower RMSE.

Discussion

Summary

A small-tip-angle k-space domain parallel transmit pulse design algorithm was proposed that divides up the calculation of a matrix relating a target excitation pattern to the pulses that produce it into a set of independent problems for patches of target excitation k-space locations, each of which is influenced by a local neighborhood of points on the excitation k-space trajectory. The division of the problem into patches of target locations creates an opportunity for fine parallelization, while the limited neighborhood sizes lead to small problem sizes for each patch. Compared to the original k-space-based algorithm of Ref. [1], the L-curve and matrix size results showed that the new algorithm produces much smaller matrix sizes that can be calculated more quickly, with the tradeoff of increased excitation error or RF power. Results showed that the algorithm also enables compensation of off-resonance which has not previously been described in a k-space domain design. Compared to a spatial domain design, the new algorithm is non-iterative and can be finely parallelized to achieve shorter design times, and results showed that it can use coarser target grid sizes while avoiding Gibbs ringing, again with the tradeoff of increased excitation error or RF power. The performance of off-resonance-compensated spatial domain and k-space domain pulse designs was similar, and the methods were similarly sensitive to excitation k-space undersampling. While all the pulse designs in this work used 3D SPINS trajectories, the method can be applied in any number of dimensions and with any excitation k-space trajectory. The MATLAB implementation described can be used for any two- or three-dimensional pulse design without modification.

R1.2

Applications and Extensions

This work was initially motivated by the observation that spatial domain parallel pulse designs can be very slow for 3D problems with large grid sizes, requiring many iterations with considerable computation per iteration. It is anticipated that the proposed k-space domain algorithm will be most useful for these types of large >2D problems, which include 3D spatial designs [11, 12] and 2D

and 3D spatial-spectral designs [13–16] where full matrix construction and inversion is infeasible due to the problem size, and an iterative design can require several minutes to solve. Furthermore, R1.7 unlike an iterative spatial domain design the proposed algorithm does not need to be repeated if the target pattern changes. This means it could have a considerable computational speed advantage for Gerchberg-Saxton magnitude least-squares pulse designs [3, 19] which alternate between designing pulses and updating a complex-valued target pattern. Such a design method would allow the user to specify only the magnitude of the target pattern, rather than magnitude and phase as was required in this work. The method could also be used to initialize spatial-domain designs to reduce the number of iterations required to reach a target cost. Finally, while simple Tikhonov RF power regularization was used in the designs presented here, more sophisticated regularization could be incorporated to, e.g., control peak RF power via adaptive regularization [27], or to enforce array compression by projecting the weights into the null space of a compression matrix [28], among other applications R1.1 [9, 10]. In such designs, it would be beneficial to pre-compute and store the lower triangular elements of the $S^H S$ matrices so they need not be re-computed as the regularization changes over iterations. R1.8 Peak power could also be controlled in k-space domain designs using parallel transmission VERSE [29] or the iterative re-VERSEit technique [30]. It is not yet clear whether R1.8, R2.2 or how hard constraints on SAR and peak- and integrated-power could be directly incorporated in the k-space method, as in Refs [20] and [21]. It may also be possible to use the k-space domain R1.8, R2.2 method to rapidly design large-tip-angle pulses via the direct linear class of large-tip-angle pulses method [31] or the additive angle method [32]; the latter alternates between small-tip-angle designs that could be solved by the k-space method, and Bloch simulations to update the target pattern. R2.3

Conclusion

The proposed k-space domain algorithm accelerates and finely parallelizes parallel transmission pulse design, with a modest tradeoff of excitation error and RMS RF amplitude.

Acknowledgments

The authors would like to thank Tianrui Luo (University of Michigan) for helpful discussions regarding Ref [23].

For Peer Review

References

[1] Katscher U, Börnert P, Leussler C, van den Brink JS. Transmit SENSE. *Magn Reson Med* 2003;49:144–150.

[2] Zhu Y. Parallel excitation with an array of transmit coils. *Magn Reson Med* 2004;51:775–784.

[3] Malik SJ, Hajnal JV. Phase relaxed localized excitation pulses for inner volume fast spin echo imaging. *Magn Reson Med* 2016;76:848–861.

[4] Mooiweer R, Sbrizzi A, Raaijmakers AJE, Van den Berg CAT, Luijten PR, Hoogduin H. Combining a reduced field of excitation with SENSE-based parallel imaging for maximum imaging efficiency. *Magn Reson Med* 2016;78:88–96.

[5] Zhang Z, Yip CY, Grissom W, Noll DC, Boada FE, Stenger VA. Reduction of transmitter B1 inhomogeneity with transmit SENSE slice-select pulses. *Magn Reson Med* 2007;57:842–847.

[6] Cloos MA, Boulant N, Luong M, Ferrand G, Giacomini E, Le Bihan D, Amadon A. k_T -Points: Short three-dimensional tailored RF pulses for flip-angle homogenization over an extended volume. *Magn Reson Med* 2011;67:72–80.

[7] Deng W, Yang C, Alagappan V, Wald LL, Boada FE, Stenger VA. Simultaneous z-shim method for reducing susceptibility artifacts with multiple transmitters. *Magn Reson Med* 2009;61:255–259.

[8] Grissom WA, Yip CY, Zhang Z, Stenger VA, Fessler JA, Noll DC. Spatial domain method for the design of RF pulses in multicoil parallel excitation. *Magn Reson Med* 2006;56:620–9.

[9] F. Padormo, A. Beqiri, J. V. Hajnal, and S. J. Malik. Parallel transmission for ultrahigh-field imaging. *NMR Biomed* 2016; 29(9):1145–1161.

[10] C. M. Deniz. Parallel transmission for ultrahigh field MRI. *Top Magn Reson Imaging* 2019; 28(3):159–171.

- [11] Malik SJ, Keihaninejad S, Hammers A, Hajnal JV. Tailored excitation in 3D with spiral nonselective (SPINS) RF pulses. *Magn Reson Med* 2012;67:1303–1315.
- [12] Davids M, Schad LR, Wald LL, Guerin B. Fast three-dimensional inner volume excitations using parallel transmission and optimized k-space trajectories. *Magn Reson Med* 2016; 76:1170–1182.
- [13] K. Setsompop, V. Alagappan, B. A. Gagoski, A. Potthast, F. Hebrank, U. Fontius, F. Schmitt, L. L. Wald, and E. Adalsteinsson. Broadband slab selection with b_1^+ mitigation at 7T via parallel spectral-spatial excitation. *Magn Reson Med* 2009; 61:493–500.
- [14] S. J. Malik, D. J. Larkman, D. P. O'Regan, and J. V. Hajnal. Subject-specific water-selective imaging using parallel transmission. *Magn Reson Med* 2010; 63(4):988–997.
- [15] Stenger VA, Boada FE, Noll DC. Three-dimensional tailored RF pulses for the reduction of susceptibility artifacts in T_2^* -weighted functional MRI. *Magn Reson Med* 2000;44:525–531.
- [16] Yang C, Deng W, Alagappan V, Wald LL, Stenger VA. Four-dimensional spectral-spatial RF pulses for simultaneous correction of B_1^+ inhomogeneity and susceptibility artifacts in T_2^* -weighted MRI. *Magn Reson Med* 2010;64:1–8.
- [17] Orzada S, Solbach K, Gratz M, Brunheim S, Fiedler TM, Johst S, Bitz AK, Shooshtary S, Abuelhaija A, Voelker MN, Rietsch SHG, Kraff O, Maderwald S, Flöser M, Oehmigen M, Quick HH, Ladd ME. A 32-channel parallel transmit system add-on for 7T MRI. *PLOS ONE* 2019;14:1–20.
- [18] Deng W, Yang C, Stenger VA. Accelerated multidimensional radiofrequency pulse design for parallel transmission using concurrent computation on multiple graphics processing units. *Magn Reson Med* 2011;65:363–369.
- [19] Setsompop K, Wald L, Alagappan V, Gagoski B, Adalsteinsson E. Magnitude least squares

optimization for parallel radio frequency excitation design demonstrated at 7 Tesla with eight channels. *Magn Reson Med* 2008;59:908–915.

[20] Brunner DO, Pruessmann KP. Optimal design of multiple-channel RF pulses under strict power and SAR constraints. *Magn Reson Med* 2010;63:1280–1291.

[21] Hoyos-Idrobo A, Weiss P, Massire A, Amadon A, Boulant N. On variant strategies to solve the magnitude least squares optimization problem in parallel transmission pulse design under strict SAR and power constraints. *IEEE Trans Med Imag* 2014;33:739–748.

[22] Grissom WA. k-Space domain parallel transmit pulse design. In *Proceedings 26th Scientific Meeting, International Society for Magnetic Resonance in Medicine, Paris. 2018*; p. 3396.

[23] Luo T, Noll DC, Fessler JA, Nielsen JF. A GRAPPA algorithm for arbitrary 2D/3D non-Cartesian sampling trajectories with rapid calibration. *Magn Reson Med* 2019;82:1101–1112.

[24] Fessler JA, Lee S, Olafsson VT, Shi HR, Noll DC. Toeplitz-based iterative image reconstruction for MRI with correction for magnetic field inhomogeneity. *IEEE Trans Sig Proc* 2005; 53:3393–3402.

[25] Lustig M, Kim SJ, Pauly JM. A fast method for designing time-optimal gradient waveforms for arbitrary k-space trajectories. *IEEE Trans Med Imag* 2008;27:866–873.

[26] Fessler JA, Sutton BP. Nonuniform fast Fourier transforms using min-max interpolation. *IEEE Trans Sig Proc* 2003;51:560–574.

[27] Yip CY, Fessler JA, Noll DC. Iterative RF pulse design for multidimensional, small-tip-angle selective excitation. *Magn Reson Med* 2005;54:908–917.

[28] Cao Z, Yan X, Grissom WA. Array-compressed parallel transmit pulse design. *Magn Reson Med* 2016;76:1158–1169.

- [29] D. Lee, W. A. Grissom, M. Lustig, A. B. Kerr, P. P. Stang, and J. M. Pauly. VERSE-guided numerical RF pulse design: A fast method for peak RF power control. *Magn Reson Med* 2012; 67:353–362.
- [30] D. Lee, M. Lustig, W. A. Grissom, and J. M. Pauly. Time-optimal design for multidimensional and parallel transmit variable-rate selective excitation. *Magn Reson Med* 2009, 61(6):1471–1479.
- [31] D. Xu, K. F. King, Y. Zhu, G. C. McKinnon, and Z.-P. Liang. Designing multichannel, multidimensional, arbitrary flip angle RF pulses using an optimal control approach. *Magn Reson Med* 2008, 59(3):547–560.
- [32] W. A. Grissom, C. Y. Yip, S. M. Wright, J. A. Fessler, and D. C. Noll. Additive angle method for fast large-tip-angle RF pulse design in parallel excitation. *Magn Reson Med* 2008, 59(4):779–87.

1
2
3
4
5
6
7
8
9
10
11
12
13
14
15
16
17
18
19
20
21
22
23
24
25
26
27
28
29
30
31
32
33
34
35
36
37
38
39
40
41
42
43
44
45
46
47
48
49
50
51
52
53
54
55
56
57
58
59
60

Table Captions

Table 1: W matrix sizes in gigabytes (GB) versus inclusion width in cycles/FOV. An inclusion width of ∞ corresponds to a full matrix solution.

For Peer Review

Figure Captions

Figure 1: (a) A target point \vec{k}_j and the nearby trajectory points that are included when calculating RF pulse weight contributions from this point. Inclusion width is defined as the distance from each target location \vec{k}_j within which all trajectory points are considered when solving for the j -th column of the design (\mathbf{W}) matrix. (b) Calculation of the \mathbf{W} matrix can be performed column-by-column for each target location \vec{k}_j , or patches of target points can be solved for jointly. Here the 16 columns of \mathbf{W} for a 4×4 patch of target points are solved together, and an inclusion width of 4 cycles/FOV dictates that all trajectory points within a 12×12 region centered on the patch are considered in the calculation.

Figure 2: The 24-channel loop Tx array that was simulated in a human head model to obtain B_1^+ maps. The array has diameter 32 cm and height 28 cm. The 16 cm \times 11 cm rectangular loops are arranged in 3 rows of 8.

Figure 3: (a) Middle axial, sagittal, and coronal slices of the target excitation pattern used for all pulse designs. (b) The SPINS trajectory used in the designs. (c) 10 ms minimum-time gradient waveforms that produce the SPINS trajectory.

Figure 4: Normalized excitation patterns (top row) and error maps (bottom row) in central axial, sagittal and coronal slices for k-space domain (left) and spatial domain designs (right).

Figure 5: (a) k-Space computation time versus number of parallel threads, for patch and inclusion widths of 4 cycles/FOV. (b) Computation time (blue axis) and RMSE (red axis) versus patch width, for an inclusion width of 4 cycles/FOV and 16 threads. (c) Computation time (blue axis) and RMSE (red axis) versus inclusion width, for patch widths of 4 and 8 cycles/FOV, and 16 threads.

Figure 6: L-curves for spatial domain and k-space domain pulse designs, repeated across five orders of magnitude of the methods' Tikhonov regularization parameters. The k-space domain designs were repeated using patch and inclusion widths of four versus solving for the entire domain at once ('Patch / Inclusion Widths = 4' versus 'Patch / Inclusion Widths = ∞ '), and using B_1^+ map product interpolation versus phase modulation to each trajectory location ('Interpolated Matrices' versus 'Exact Matrices').

Figure 7: Normalized error maps and RMSEs for (a) pulses designed using a trajectory that reaches 6 mm isotropic resolution and the spatial domain algorithm with a $32 \times 32 \times 24$ grid, (b) pulses designed using the same trajectory and the spatial domain algorithm with a $64 \times 64 \times 48$ grid, and (c) pulses designed using the same trajectory and the k-space domain algorithm with a $32 \times 32 \times 24$ design grid. Red arrows indicate Gibbs ringing in the $32 \times 32 \times 24$ spatial domain design.

Figure 8: Normalized error maps, RMSEs, and computation times for spatial domain design (first row) and k-space domain design (second row), using excitation k-space trajectories with different reduction factors (third row). The reduction factors are referenced to the 10 ms trajectory in Figure 3 (second column).

Figure 9: (a) Normalized off-resonance map containing a Gaussian distortion centered above the frontal sinus, to mimic air-tissue susceptibility difference-induced B_0 inhomogeneity. (b) Normalized excitation maps and RMSEs for spatial domain design with off-resonance correction (first row), and k-space domain design without and with off-resonance correction (second and third rows).